JGR Space Physics

RESEARCH ARTICLE
10.1029/2019JA027271

Key Points:

- Earth's magnetospheric N_2^+, NO^+, and O_2^+ (~43%, ~46%, and ~10%, respectively) argue for ionospheric ion outflow at ~350–550-km altitude
- Outside Earth and Saturn's magnetospheres, levels of heavy molecular (atomic) ions relative to O^+ are higher (similar) compared to inside
- Heavy molecular to lunar atomic pickup ion ratios are >>1, ~1, and <1 in Earth's magnetosphere, the sheath, and the solar wind, respectively

Supporting Information:

- Supporting Information S1

Correspondence to:
S. P. Christon,
spchriston@aol.com

Citation:
Christon, S. P., Hamilton, D. C., Mitchell, D. G., Plane, J. M. C., & Nylund, S. R. (2020). Suprathermal magnetospheric atomic and molecular heavy ions at and near Earth, Jupiter, and Saturn: Observations and identification. *Journal of Geophysical Research: Space Physics*, *125*, e2019JA027271. https://doi.org/10.1029/2019JA027271

Received 7 AUG 2019
Accepted 14 NOV 2019
Accepted article online 15 DEC 2019

Suprathermal Magnetospheric Atomic and Molecular Heavy Ions at and Near Earth, Jupiter, and Saturn: Observations and Identification

S. P. Christon[1], D. C. Hamilton[2], D. G. Mitchell[3], J. M. C. Plane[4], and S. R. Nylund[3]

[1]Focused Analysis and Research, Charleston, SC, USA, [2]Department of Physics, University of Maryland, College Park, MD, USA, [3]Johns Hopkins University Applied Physics Laboratory, Laurel, MD, USA, [4]School of Chemistry, University of Leeds, Leeds, UK

Abstract We examine long-term suprathermal, singly charged heavy ion composition measured at three planets using functionally identical charge-energy-mass ion spectrometers, one on Geotail, orbiting Earth at ~9–30 Re, the other on Cassini, in interplanetary space, during Jupiter flyby, and then in orbit around Saturn. O^+, a principal suprathermal (~80–220 keV/e) heavy ion in each magnetosphere, derives primarily from outflowing ionospheric O^+ at Earth, but mostly from satellites and rings at Jupiter and Saturn. Comparable amounts of Iogenic O^+ and S^+ are present at Jupiter. Ions escaping the magnetospheres: O^+ and S^+ at Jupiter; C^+, N^+, O^+, H_2O^+, $^{28}M^+$ (possibly an aggregate of the molecular ions, MI, CO^+, N_2^+, $HCNH^+$, and/or $C_2H_4^+$), and O_2^+ at Saturn; and N^+, O^+, N_2^+, NO^+, O_2^+, and Fe^+ at Earth. Generally, escaped atomic ions (MI) at Earth and Saturn have similar (higher) ratios to O^+ compared to their magnetospheric ratios; Saturn's H_2O^+ and Fe^+ ratios are lower. At Earth, after O^+ and N^+, ionospheric origin N_2^+, NO^+, and O_2^+ (with proportions ~0.9:1.0:0.2) dominate magnetospheric heavy ions, consistent with recent high-altitude/latitude ionospheric measurements and models; average ion count rates correlate positively with geomagnetic and solar activity. At ~27–33 amu/e, Earth's MIs dominate over lunar pickup ions (PUIs) in the magnetosphere; MIs are roughly comparable to lunar PUIs in the magnetosheath, and lunar PUIs dominate over MIs beyond Earth's bow shock. Lunar PUIs are detected at ~39–48 amu/e in the lobe and possibly in the plasma sheet at very low levels.

Plain Language Summary Some of the air we breathe, a gas of ~78% N_2 and ~21% O_2 molecules, expands into the high-altitude atmosphere, the thermosphere, and becomes ionized by sunlight and charged particles from space to become the ionosphere. Molecules can break up into their component atoms or combine with other ions to form other molecules. Some ionospheric ions flow out into space, mostly during geomagnetic disturbances, and are further energized. Magnetospheres, plasma bubbles filled with these energized particles, form around planets with magnetic fields, like the Earth whose magnetic field stands off the steady stream of ions and electrons from the Sun called the solar wind. Particles inside the bubbles can be planet or satellite origin, and outside the bubble, they are mostly Sun origin. However, some inside get out and some outside get in. Improved ion measurements from space give us information to help unravel both the outflowing particles' interactions on the way out and when and how ions escape or penetrate magnetospheres. Planets' satellites and rings also contribute ionized and neutral particles to the mix, making various determinations more difficult than others. Ions from solar wind and sunlight impacting Earth's satellite, the Moon, which spends most of its time outside Earth's magnetosphere, dominate ion composition at some masses and energies there while contributing little overall inside. In contrast, many of Jupiter and Saturn's satellites spend most of their time inside their planets' magnetospheres and contribute significantly to their particle populations. This study, focused on singly charged heavy molecular ions, compares the composition of ions with masses from carbon to iron in and near the magnetospheres of Earth, Jupiter, and Saturn, attempting to unravel some compositional information.

1. Introduction

A comparison of predominantly singly charged heavy ion composition in and near the magnetospheres of Earth, Jupiter, and Saturn is presented in order to (a) more clearly identify, better characterize, and fully understand the different magnetospheric heavy atomic ion and molecular ion (MI) populations of the three magnetospheres and (b) demonstrate and characterize the uniquely different responses to atomic and molecular ions provided by the time-of-flight, total-energy ion spectrometers used in this and numerous other studies. These two objectives are intertwined and interdependent, so that either one cannot clearly be presented without significant cross referencing; therefore, both are addressed herein, rather than separately. Our focus is on singly charged ions as they represent the primary, most statistically significant component of ionospheric outflow, but note that not all ions flowing out of planetary ionospheres or escaping magnetospheres are singly charged; some are doubly and possibly triply charged. The first observations of suprathermal MI in Earth's ring current and near-Earth lunar pickup ions (PUI) were made with this class of instrument by Klecker et al. (1986) and Hilchenbach et al. (1992), respectively. That Earth's ionosphere contributes significantly to its magnetospheric O^+ and H^+ ion populations known from persistent investigation and repeated observation (see e.g., Moore et al., 2014; Shelley et al., 1972; Strangeway et al., 2005; Yau et al., 1993, 2011, 2012, and references therein). Twenty-four years ago, Peterson et al. (1994) noted: “Twenty years after the discovery that significant fluxes of O^+ flow out of the ionosphere (Shelley et al., 1972), there exists little or no quantitative information about the relative importance of the various physical processes responsible for the energization and extraction of O^+ and other heavy ions from the Earth's ionosphere.” Now, nearly a quarter of a century later, although continual research (e.g., Andersson et al., 2004; Foss et al., 2017; Haaland et al., 2012; Moore et al., 2014; Ogawa et al., 2010; Peterson et al., 1994; Redmon et al., 2014; Seki et al., 2019; Shen et al., 2018; Skjæveland et al., 2014; Strangeway et al., 2005; Wilson et al., 2004; Yau et al., 1993, 2011; Yu & Ridley, 2013) has clarified much about thermospheric/ionospheric ion upflow, downflow, outflow, and chemistry, there is still much to be learned. The study of Earth's MI populations remains important in that much of the extant O^+ in its magnetosphere is affected by the altitude and local time of MI interactions during outflow. Likewise, the origination location of MI populations at Jupiter and Saturn determines the level of dissociation that creates a number of the atomic ion populations there. Various disturbances in both the Sun and the interplanetary medium can result in significant planetary magnetospheric responses such as Earth's geomagnetic storms and substorms, which directly affect the planet's thermosphere, ionosphere, and magnetosphere and the extant particle populations, both ionized and neutral, therein. Effects including enhanced upward neutral winds, plasma wave activity during disturbed conditions at and above ~110-km altitude, and *F* region altitude variations occur from low to high geographic latitudes before, during, and after the more intense phases of magnetospheric disturbances (see, e.g., Price & Jacka, 1991; Danilov & Lastovica, 2001; Goncharenko et al., 2004; Blagoveshchenskii, 2013). In composing this paper, our attempt to keep the length, range, and scope of the paper focused, limited its range to singly charged heavy ions with atomic masses of >10 amu. Nevertheless, the presence or possible presence of escaped higher charge state (+2 and +3) magnetospheric ions in the nearby magnetosheath and/or solar wind is demonstrated herein in Supporting Information figures: Earth: S3a and S3b; Jupiter: 1b and 3; and Saturn: S3f.

While progress on many details regarding outflow has been made, that is, the models are better and there are more observations fostering better understanding, we still appear to lack some important ion composition information from the upper ionosphere/thermosphere that might help us better understand and characterize ionospheric outflow at Earth. That is, beyond the overview of the Yau et al. (1993) data by Peterson et al. (1994) and the very recent high-altitude measurements by Foss et al. (2017) and the ring current measurements by Seki et al. (2019), there has been little resolution of the vertical interactions affecting ions during outflow. To our knowledge the literature still does not present an overall consensus as to what chemistry and which processes/conditions/mechanism(s) at what latitudes and altitudes result in the variability of outflowing ionospheric ions (see, e.g., Welling & Liemohn, 2016). For example, in the recent statistical study by Shen et al. (2018) of electromagnetic-wave-related ion heating at ~350–700-km altitude, the majority of ionospheric ion heating events were found to be associated with core ion downflows rather than upflows. Only recently has quantitative in situ observational assessment of the relative contributions of ${N_2}^+$, NO^+, and ${O_2}^+$, three fundamental components of ionospheric chemistry, been revisited by Foss et al. (2017), who reported conclusions generally consistent with the earlier result from Yau et al. (1993) and Peterson et al. (1994) that ionospheric ${O_2}^+$ is a minor constituent at ~400-km altitude. In the ring current at $3.5 \leq L < 6.6$ (where L is McIlwain's L parameter), Seki et al. (2019) find that keV-energy MI are commonly observed during geomagnetically active periods associated with magnetic storms, substorms, and high-speed solar wind streams; the MIs are not detected above background levels in the ring current during quiet intervals, and their detection probability increases with increasing geomagnetic disturbance level. Our paper cannot identify the causes or details of outflow processes because the outflow energization processes are at core (sub-keV) plasma energies in the high ionosphere/thermosphere, energies and regions we do not sample. However, Geotail, which orbits at several to tens of planetary radii, carries our instrumentation, which measures suprathermal energy, ~80–200 keV, ions in the high-energy tail of ion distributions. This instrumentation provides information on the relative abundances of the MI that have flown out of the ionosphere. Cassini's complementary observations at Jupiter and Saturn provide us not only with clarifying observational evidence about the number and composition of suprathermal heavy ions that populate their magnetospheres but also with several critical observations, which help improve our understanding of both instruments' responses at all three planets. The information provided herein may provide incentive for various future-focused investigations of Earth's ionosphere and thermosphere using new or existing instrumentation and measurements.

Two years of ion composition observations from the AMPTE/CCE spacecraft demonstrated that after O^+, N^+ is the next most important ionospheric origin ion in the storm time ring current (Gloeckler & Hamilton, 1987). Regardless of this, most studies of terrestrial ionospheric heavy ion outflow to this day discuss one heavy ion species, O^+, completely ignoring N^+ (e.g., Mall et al., 2002; Christon et al., 2002; Ilie & Liemohn, 2016), knowledge of which is important in understanding the chemistry of Earth's outflow processes. At suprathermal energies in the outer ring current-to-plasma-sheet region, Christon et al. (2002) find that the average flux ratio of escaped N^+ relative to O^+ is ~40% (~20%) during solar minimum (maximum). Using Geotail/STICS data, they found that at $\gtrsim$9–10 Re during solar minimum, the average dayside ~10–210 keV/e N^+/O^+ flux (PHA) ratio is ~0.36–0.40 (~0.38–0.42) over ~1–2 years, with N^+/O^+ ~1 for ~18 hr on one contributing Geotail orbit, while during solar maximum, the average N^+/O^+ flux (PHA) ratio is ~0.22–0.23 (~0.24–0.26) over ~1–2 years. In a collaborative companion study, Mall et al. (2002) used concurrent Wind/STICS data to find that the average nightside ~8–38 Re magnetospheric ~10–210 keV/e N^+/O^+ density ratio was ~0.45–0.6 from 1995 to 1997 (solar minimum) and decreases in 1997 monotonically to ~0.20–0.23 where it remained from 1998 through mid-2000 (solar maximum). The two studies, taken together, clearly demonstrate solar cycle and radial variations of N^+ relative to O^+. In a somewhat comparable situation, escaped ionospheric MIs were discovered in the outer ring current by Klecker et al. (1986) and identified as NO^+ and ${O_2}^+$. This MI composition was in contrast to an earlier report by Craven et al. (1985) from polar cap observations at ~1.1–3 Re geocentric that ${N_2}^+$ and NO^+ dominated over ${O_2}^+$ at higher altitudes and latitudes. This difference was considered inconsequential as Craven et al. postulated that the ${N_2}^+$ and NO^+ dominance might be seasonal since there was no overall consensus at that time in the relative abundance of ${O_2}^+$ in earlier high-altitude observations. The empirical model of Köhnlein (1989) used observations from six satellites to show ${O_2}^+$, a major constituent below 100–200 km, falling off more quickly at higher altitudes than ${N_2}^+$ and NO^+. Later, Hoegy et al. (1991) summarized a number of ionospheric data and/or model studies, showing that the densities of both ${N_2}^+$ and NO^+ were likely to be somewhat greater than that of ${O_2}^+$ at altitudes of ~400–600 km. Subsequent MI composition consistent with the Craven et al. (1985) and Hoegy et al. (1991) results was reported by Yau et al. (1993) at ~2–4 Re in a study of mass spectrometer data obtained on hundreds of ionospheric high-altitude, high-latitude satellite passes. The complementary comprehensive studies by Yau et al. (1993) and Peterson et al. (1994) clearly identified ${N_2}^+$ and NO^+ as the principal, comparably abundant, outflowing ionospheric Mass-30 (~27–33 amu) molecular ion species in high-latitude, high-altitude measurements at 2–3 Re. Yau et al. (1993) reported ${O_2}^+$ to be about an order of magnitude smaller, and Peterson et al. (1994) chose to not discuss ${O_2}^+$ in their study.

Christon, Gloeckler, et al. (1994) and Christon, Hamilton, et al. (1994) referred to escaped ionospheric MI in Earth's magnetosphere as NO^+ and ${O_2}^+$, reflecting the earlier observations and identification by Klecker et al. (1986) and Gloeckler and Hamilton (1987). The characteristics of MI energy loss processes in the instruments of the 1994 studies (in one, the instrument used herein, and the other, a similar instrument) were not clearly understood at the time. As discovered and presented in this and recent investigations (Christon, Hamilton, DiFabio, et al., 2013; Christon et al., 2015), we now understand that atomic and molecular ion energy loss measurements in this class of time-of-flight total-energy instrument must be analyzed differently. Based on the comparisons and evidence presented in this paper, which utilizes two nearly identical charge-energy-mass ion spectrometers in three different magnetospheres, we now more fully understand

and are better able to more clearly identify and characterize the heavier-than-oxygen suprathermal MI populations at these planets using this class of instrumentation. Singly charged heavy ion populations and their measurement using time-of-flight instruments will hopefully be more clearly understood at all three planets as a result of this study. The improved composition assessment of the long-term MI component of outflown ionospheric MI fluxes observed in Earth's magnetosphere presented herein is intended to help focus planning choices for future thermosphere-ionosphere-magnetosphere observations.

The Geotail suprathermal charged particle data set at Earth contains multidecadal measurements of ionospheric origin heavy ions that have flown out of Earth's ionosphere into the magnetosphere and some that escape and travel sunward of Earth's bow shock, into the interplanetary medium (see, e.g., Christon et al., 2000). A primary purpose of this paper is to clearly identify which MI ultimately flow out of Earth's ionosphere and are subsequently incorporated into Earth's magnetospheric ion population. This identification is facilitated by results from the other primary purpose of this paper, a direct comparison of heavy ion observations at Earth with those at Saturn and Jupiter. In fulfilling these goals, we also address the fate of escaped MI after they leave the protection of the planetary magnetospheres. A factor in and consequence of this study is the recognition that suprathermal lunar pickup ions, PUIs, from the solar wind interaction with Earth's satellite, the Moon, are readily detected in the solar wind from outside the magnetopause to near the Moon. At the lunar distance (~60 Re) sunward of Earth, the solar wind interacts with the Moon, its exosphere, and its dust environment (McComas et al., 2009). Additionally, the solar wind interacts with the terrestrial exosphere whose H component, at least, extends to geocentric radial distances of ~100 Re (Baluikin et al., 2019). Further, to our knowledge, little is established about the composition or distance distribution of either Earth's outwardly traveling energetic neutral atom populations. Note that Earth's exosphere is modeled at low altitudes presuming a six-component exosphere containing H, He, N, O, N_2, and O_2 (see, e.g., McKenna-Lawlor et al., 2005). That solar wind interactions with the Moon produce PUIs have been established by a quarter century of lunar ion observations sunward of Earth, both near Earth (e.g., Hilchenbach et al., 1992) and near the Moon (e.g., Halekas et al., 2015; Kirsch et al., 1998; Mall et al., 1998). Heavy lunar PUIs are observed to contain at least ~12–42 amu/e ions, primarily of O^+, Si^+, Al^+, P^+, and Ca^+ (Hilchenbach et al., 1992; Kirsch et al., 1998; Mall et al., 1998) and possibly ${CO_2}^+$ (Tanaka et al., 2009), while secondary ion mass spectroscopy of lunar soil simulant samples (Elphic et al., 1991) and actual Apollo regolith samples (Dukes & Baragiola, 2015), that is, the loose surface material covering solid rock, defines a broader range of expected PUIs, additionally including atomic: Na^+, Mg^+, Al^+, Si^+, P^+, K^+, Ca^+, Ti^+, Mn^+, and Fe^+, and molecular: $^{43}AlO^+$, $^{44}SiO^+$, $^{64}TiO^+$, and $^{72}FeO^+$ ions. Of note, Earth's ionospheric meteoric metal neutral and ion layers at ~80–120 km altitude include Na, Mg, Al, Si, K, Ca, Ti, and Fe (Plane et al., 2018), many of the expected lunar PUIs (see also our discussions in Christon et al., 2015, 2017). These metals and important molecules are found in the cosmic dust that forms the zodiacal cloud, a circumsolar disk of small particles and debris produced by asteroid collisions and sublimating comets (Carrillo-Sánchez et al., 2016; Bridges et al., 2010) that extends to ≥10 AU (Nesvorný et al., 2010; Poppe, 2016). The main components of the cometary ices that contribute to cosmic dust are H_2O (~80% by number) followed by CO and CO_2 (Bockelée-Morvan, 2011). Therefore, the observation of any of these atomic or molecular ions near Earth may not necessarily suggest their source, the Moon or Earth's ionosphere, both of which have been impacted by cosmic dust for billions of years. Concerted investigations for certain ion species have led to null results, as in the case of lunar Fe^+, which has been sought, but not measured in at least two studies, Hilchenbach et al. (1992) and Kirsch et al. (1998), both using instrumentation similar to that used herein. We find that in our current, all-inclusive data set measured in Earth's equatorial magnetosphere (including from the $R < {\sim}30$ Re plasma sheet and the outer quasi-trapping regions at $R > {\sim}9$ Re, dayside and nightside), lunar PUIs are not obviously present at levels above the resident terrestrial ion populations therein. In fitting background subtracted Mass-30 ions in the magnetosphere, we show below that inclusion of low levels of Si^+ produces negligible effects on the resulting Mass-30 ion distribution. Finally, our observations are consistent with the understanding that Earth is the only one of these three planets where the planet's ionosphere appears to supply the majority of the locally originated heavy ions on the average. While Saturn and Jupiter's magnetospheric heavy ion populations likely originate primarily from their satellites, rings, and/or dust/neutral/ion tori, the Moon does not appear to contribute significantly to Earth's observed magnetospheric suprathermal ion populations in the ~27–33-amu mass range focused on herein. However, we find that higher-mass lunar-and-or-ionosphere species ions are present in the magnetosphere. Outside the magnetopause, lunar ions are readily detected, whereas inside the magnetospheric plasma sheet region, they are not definitively detected, although they are probably present. These intertwined topics are the subject of this paper.

Suprathermal Mass-30 ion populations in Earth, Jupiter, and Saturn's magnetospheres are distinct and different. MIs in the Mass-30 range are minor components of Earth's total ionospheric contribution to suprathermal ion populations in the magnetosphere and the nearby interplanetary medium, superseded by the atomic ions H^+, He^+, O^+, and N^+ (e.g., Gloeckler & Hamilton, 1987). Comparison of the suprathermal heavy ion measurements from the three planets allows us to utilize the abundant Jovian S^+ measurement peak as a fiducial at 32 amu/e, which, when combined with the uncomplicated observations of MI escape from Saturn's magnetosphere, allows us to more clearly identify Earth's magnetospheric MI populations. These observational tools, fiducial and patterned response, have enabled us to better understand the measurements at Earth, allowing us in some situations to separate the ionospheric origin molecular ions N_2^+, NO^+, and O_2^+ from ionospheric origin atomic metal layer ions, including Al^+ and Si^+, and atomic lunar PUIs, including Al^+, Si^+, and P^+, (all with mass numbers between 27 and 31) in near-Earth plasmas with a cautious level of confidence. At Saturn, we report the first detailed observations of Saturn's H_2O^+, $^{28}M^+$, and O_2^+ in the interplanetary medium. At Jupiter, no MI from Io or the Galilean satellites appear to survive its intense inner magnetosphere particle radiation environment, except possibly a trace of CO_2^+, which may be introduced by cosmic dust from the Jupiter family comets (Bockelée-Morvan, 2011). Jovian O^+ and S^+, likely dissociated primarily from Io's molecules and its torus' SO_2, dominate the heavy ion population of Jupiter's magnetosphere. Jupiter's S^+ extends far into the near ~5-AU (astronomical unit) interplanetary medium. At Earth, we demonstrate that primarily N_2^+ and NO^+, but also a detectable, non-negligible amount of O_2^+, flow out into the magnetosphere. We search for lunar PUIs in Earth's equatorial plasma sheet and outer quasi-trapping regions. We provide general information on the overall MI distribution in the ~9–30 Re near-Earth region and the average MI relation to geomagnetic and solar activity. Overall, MI and their dissociation products might play more of a role in magnetospheric dynamics at Jupiter and Saturn than at Earth.

Four molecular ions at Saturn, CO^+, N_2^+, $HCNH^+$, and $C_2H_4^+$, have now been suggested or identified in particle fluxes at Saturn that could possibly contribute to the ubiquitous suprathermal heavy ion signal with an atomic mass of 28 amu that is observed in and near Saturn's magnetosphere (Waite et al., 2009; Westlake, Paranicas, et al., 2012; Mandt et al., 2012; Postberg et al., 2018). CO, N_2, and HCNH are among the molecules with the strongest chemical bonds in chemistry (Kalescky et al., 2013). Once released somewhere in Saturn's magnetosphere, either near Saturn's rings, Enceladus, or Titan, any one of the three should likely persist long enough to ionize (if neutral on release), circulate, and be accelerated to suprathermal energies. The high bond strengths of these ions suggest that they are probably less prone to UV photolysis, although the bond strength will have almost no effect on the rate of dissociative recombination with electrons, which may be the process that controls their lifetimes closer to Saturn. Waite et al. (2006, 2009) argued that the dominant neutral 28-amu thermal energy molecule in the Enceladus plume was more likely N_2 or C_2H_4 rather than CO, citing corroborating measurements from other Cassini instruments. Note though that some of the relatively abundant CO_2 in the Enceladus plumes (Postberg et al., 2018; Waite et al., 2006, 2009) might evolve into the observed CO^+ through dissociation in the high-energy charged particle environment near ~4 R_S. $HCNH^+$, the most abundant ion in Titan's ionosphere (Westlake, Waite, et al., 2012), is also the dominant ion observed flowing out of Titan's exobase (Westlake, Paranicas, et al. (2012). Given the observed N^+ outflow component, Titan's $HCNH^+$ was estimated to be ~10 times more abundant than N_2^+ in the outflow. Therefore, $HCNH^+$ likely dominates Titan's toroidal wake, if one exists. Early predictions of Saturn's ion populations envisioned a torus derived from N_2-rich Titan near its orbit, similar to the Enceladus water-group torus. Although a Titan torus has not yet been clearly distinguished in Cassini data (Smith & Rymer, 2014), work to characterize plasmas near Titan (Woodson et al., 2015) continues. An attractive aspect of $HCNH^+$ is that its dissociation could easily yield comparable numbers of N-rich and C-rich fragments contributing to the comparable abundances of suprathermal C^+ and N^+ observed in Saturn's magnetosphere (Mauk et al., 2009; Christon, Hamilton, Difabio, et al, 2013; Christon, Hamilton, Mitchell, et al., 2013; DiFabio, 2012). To our knowledge, the origination processes for CO^+ and N_2^+ at Saturn are unknown, and $HCNH^+$ might or might not survive high-altitude chemical interactions to escape from Titan. Saturn's major suprathermal heavy ions W^+, (O^+, OH^+, and H_2O^+), assumedly from Enceladus, and O_2^+, assumedly from the main rings, are obviously energized from thermal origination. Similar overall energization processes should also affect Titan-origin ions. Preliminary radial variations of suprathermal $^{28}M^+$ (Figure S15 in the Supporting Information) appear more similar to those of suprathermal O_2^+ than W^+ at ~8–20 Rs. That being said, the fundamental test for species identification is instrumentation. However, to our knowledge, there is no current spaceborne instrumental capability in use to clearly identify and separate these four Mass-28 molecules. This capability is needed in order to identify one or two candidates as more likely dominant than the others. Therefore, herein, we will again simply identify those molecular ions at Saturn with an atomic mass of 28 amu as Mass-28 ions, or $^{28}M^+$, in this paper as in our previous papers, except in cases where discrimination as to the analytic method of identification of these ions as $^{28}Mq^+$ or $^{28}Ma^+$ is attempted.

The following section contains aspects of the spacecraft trajectories and locations, as well as instrument information. Since several important instrument measurement characteristics are only revealed through the comparison of measurements in different planetary plasma environments and, as far as we know, this will be the first time such information will appear in the literature and used in detailed observation comparisons, these characteristics are introduced and discussed in the following section. A glossary of terminology is located at the end of the paper and duplicated in the supporting information, SI. We attempt to consistently use the terms “outflow” and/or “flow out” to describe transport out of the ionosphere and reserve “escape” to describe transport out of the magnetosphere.

2. Spacecraft and Instruments

2.1. Spacecraft

We use data from the functionally identical Geotail/STICS (Supra-Thermal Ion Composition Spectrometer) and Cassini/CHEMS (CHarge-Energy-Mass Spectrometer) ion spectrometers on the Geotail and Cassini spacecraft, respectively. Geotail is an Earth-orbiting spacecraft launched in 1992, which explored Earth's deep magnetotail until early 1995, when it was placed into an equatorial ~9 × ~30 Re elliptical orbit where it provides measurements to this day. Cassini was launched from Earth in 1997 and used a Jovian gravity assist in 2001 to arrive at Saturn in mid-2004. Thereafter, Cassini was maneuvered through constantly changing orbit configurations in order to investigate various portions and aspects of Saturn's magnetospheric environs until 2017 when the spacecraft was crashed into Saturn. Data used herein were collected from both instruments for all solar and planetary activity levels. Most high background levels in our data sets likely result from the highest disturbed magnetospheric and/or solar activity intervals, which we chose to include in this initial survey of the Earth data. Specific information about the trajectories, though not essential for the focus of this paper, is provided in Figure S2 and Tables S1-S3 in the SI for reader review. Please note the distinct plasma regime labeling, which differentiates the two planets' regimes in the text and highlights their different selection procedures. Instrument information specific to Cassini/CHEMS is at https://pds-atmospheres.nmsu.edu/data_and_services/atmospheres_data/Cassini/logs/mimi_user_guide_9_26_18.pdf. The documents EPIC Instrument User's Manual (https://spdf.sci.gsfc.nasa.gov/pub/data/geotail/epic/documents/EPIC_Instrument_Users_Manual-abbr.pdf) and EPIC STICS PHA Data Product Description (https://spdf.sci.gsfc.nasa.gov/pub/data/geotail/epic/documents/EPIC_STICS_PHA_data_product_description.pdf), containing Geotail/STICS instrument information, are at https://spdf.sci.gsfc.nasa.gov/pub/data/geotail/epic/documents/.

2.1.1. Geotail

Geotail is a spinning spacecraft, with spin axis inclined sunward with an angle of 87° with respect to the solar ecliptic plane, and a spin rate is 20 rpm (Nishida, 1994). A database of 3-hr interval near-Earth plasma regime regions was constructed from contiguous 12-min interval Geotail data measurement locations in a single regime as determined by the NASA Satellite Situation Center (SSC) Spacecraft Region Identification utility in the manner described in Christon et al. (2017). Plasma regimes (and acronyms) included herein for Earth are Earth's magnetosphere (SPHERE), magnetosheath (SHEATH), and lobe (LOBE), and the nearby solar wind, interplanetary medium (SW/IM). A map of the plasma regime locations and the locations of the MI observations is plotted in Figure S1 in the SI. A smaller version of the regime map also appears below in the section on lunar PUIs near Earth. Three-hour intervals with mixed region identifications and/or including magnetospheric boundary layers are not used herein. The SPHERE, the primary plasma regime dominated by Earth's magnetic field inside the magnetopause (MP), contains the plasma sheet (PS), ring current, and near-Earth equatorial dayside locations. The low-density LOBE is roughly colocated with and lies above and below the SPHERE in the magnetotail. The SHEATH is a region of disturbed magnetic field and intermediate solar wind dominated plasmas outside the SPHERE. The magnetopause (MP) is the boundary between SPHERE and SHEATH. The outer boundary of the SHEATH is the bow shock (BS), which is the earthwardmost boundary of the generally unperturbed solar wind/interplanetary medium, SW/IM, which is dominated by outflowing solar plasma and magnetic field. As a result of its orbit and solar and geomagnetic disturbances, Geotail spends different lengths of time in each plasma regime. These livetime differences affect the observation times therein and therefore the overall relative observation totals in each regime. We do not correct for these differences in this paper, as full quantitative calculations are reserved for a future publication. Rough ratios of the total observation time in the regimes relative to that in the SPHERE are SPHERE, 1.0; LOBE, 0.1; SHEATH, 0.7; and SW/IM, 1.5; that is, there is ~50% more observation time spent in the SW/IM than in the SPHERE. We use omnidirectional measurements in this study. Please note that for representative lunar PUI samples, we utilize published measurements of lunar pickup ion composition from Hilchenbach et al. (1992), who used a similar type of ion spectrometer on AMPTE/IRM sunward of Earth's bow shock at ~18.7 Re and Mall et al. (1998), who used the WIND/STICS ion spectrometer, functionally identical to Geotail/STICS (Gloeckler et al., 1995), in a concerted campaign investigating lunar PUIs on 17 lunar flybys at >17 lunar radii. Note also that because all but one of the Kirsch et al. (1998) study's lunar orbits are likely fully included in the Mall et al. (1998) study, we do not add their data to our set of representative lunar PUI samples.

2.1.2. Cassini

Information from Cassini's interplanetary cruise to Saturn, including the Jupiter flyby, and the first 3 years of Cassini's orbits around Saturn are used in this paper. Figure S1b shows Cassini's locations from 1999-001 prior to Earth flyby, past Jupiter, to Saturn, and then at Saturn thereafter until 2017-001 in solar ecliptic coordinates. In the SI, Table S2 gives the important events during Cassini's cruise to Saturn. On Cassini's cruise to Saturn, cruise data were obtained as allowed by tracking schedules, so there was very limited data livetime, much less than when Cassini orbited Saturn. During the cruise to Saturn, the CHEMS field of view rarely included the solar direction, so the measured fluxes were not necessarily representative of the full three-dimensional interplanetary particle populations. At Saturn, Cassini, a three-axis stabilized S/C, occasionally rolled for limited intervals. Plasma regimes (and acronyms) used herein for Saturn are Saturn's magnetosphere (Sphere), magnetosheath (Sheath), and the nearby solar wind, interplanetary medium (Solar Wind). Saturn's Lobe regime is not addressed herein. Figures S1c, S1d, and S2 show the Cassini trajectory in Saturn-centered coordinates for an extended interval in which magnetopause and bow shock crossings were identified by a Cassini magnetosphere and plasma science research team (see Acknowledgements and Table S3a in the SI). The near-Saturn Solar Wind intervals used herein were collected over 28 of the longest continuous near-Saturn interplanetary samples (totaling ~170 hr) from late 2004 to late 2007 using their bow shock identifications (see Table S3 in the SI). Saturn's Sphere data were obtained in the radial range from ~4 Rs out to either (1) ~20 Rs or (2) a magnetopause crossing if it was closer (see Christon, Hamilton, DiFabio, et al., 2013, Christon et al., 2017). Intervals close to Saturn near ~4–6 Rs, when Cassini was not in nominal, magnetospheric plasma sheet-like plasmas (i.e., radiation belts) were excluded. Lists of the included and excluded $R < 20$ Rs orbit intervals used herein are in Tables S3a to S3d.

2.2. Instruments

The Geotail/STICS and Cassini/CHEMS instruments are ion charge state spectrometers using time of flight (TOF), and total energy (E), to measure singly charged heavy ions' Mass (M) and Mass per Charge (M/Q) in the ~80–200-keV/e energy range with nearly full three-dimensional measurement capabilities. Although STICS was operational before CHEMS, the instruments are very similar in design and nearly identical functionally. Geotail/STICS is described in detail most recently in Christon et al. (2017) and Cassini/CHEMS in Christon, Hamilton, DiFabio, et al., (2013; see also Williams et al., 1994; Krimigis et al., 2004, respectively). The energy range used in this paper is ~83–167 keV/e for Cassini/CHEMS and ~87–212 keV/e for Geotail/STICS. General features of both are reviewed in Tables S1–S5 in the SI in which particulars regarding launch, orbit, and cruise, deflection voltages, and onboard species rate classifications. Only new aspects and/or perspectives of the instrumentation will be described in the text. In this analysis, we have resolved several issues related to subtle differences between atomic and molecular ion measurements by this class of time of flight instrument. These differences, described in the following paragraphs, are utilized throughout the paper and reflect some supporting information presented in Christon, Hamilton, DiFabio, et al., (2013). Although H_2O^+ is presented and briefly discussed herein, full treatment of Saturn's H_2O^+ is reserved for future analysis. An additional point to note is that except for species close in mass (e.g., N_2^+, NO^+, and O_2^+), the count ratios we report cannot be interpreted as relative abundances because of decreasing detection efficiency with increasing mass, especially for molecules. This paper's primary focus is the Mass-30 diatomic molecular ions.

Electrostatic focusing selects an ion's energy-per-charge (E/Q) and guides it to pass through a thin carbon foil, and, if not widely scattered, to subsequently strike a solid-state detector (SSD). TOF measurement of each incident ion's travel from the carbon foil to the SSD, at regularly cycled deflection E/Q steps permits determination of the ions' Mass per Charge, M/Q, classification. Each ion with a TOF measurement may also have sufficient energy remaining to leave a measured residual energy deposit (Em) above the SSD's electronic threshold energy. If sufficient energy is deposited in the SSD (Em > ~25 keV, the electronic threshold), the ion will also be assigned a nonzero Mass (M) classification based on the E/Q, TOF, and Em. These physical measurement parameters, along with the known instrument state and orientation at the time of ion measurement, are called a Pulse Height Analysis event, or a PHA. The instrument's data processing unit (DPU) subsequently increments various rate counters and registers based on the E/Q, TOF, and Em of each incident ion. It also retains a limited sample of the full PHA measurement population and transmits only that sample's information to Earth as a result of telemetry bandwidth limitations. These limited, but precise, PHA samples, not the broader, actively collected counting rates, are the basis of the ability to characterize rare and/or closely intermixed ion species. Counting rates of only some ion species are collected automatically, and even these rates cannot automatically correct for spillover of one species' events into another species' rate collection box (see, e.g., Christon et al., 2002). Fluxes of various other ion species, such as those in this study, can be studied using the transmitted sample PHA information.

The classification and categorization decisions utilized by the instruments for every measured ion depend on electronically encoded M and M/Q versions of the algorithms we have used to calculate and verify instrument results in this and earlier papers (the interested reader can, for example, review these algorithms in the Geotail/EPIC Instrument User's Manual at https://spdf.sci.gsfc.nasa.gov/pub/data/geotail/epic/documents/). These algorithms convert measured incident energy per charge, TOF, and energy deposit combinations for each ion into M and M/Q values utilized in categorization decisions made by the instrument's onboard data processing unit (DPU) and discussed in this paper. Our purpose is not to analyze or revise the algorithms. They and their inherent parameters have been used and kept constant since launch of the spacecraft in the early 1990s. Our purpose is to use the instruments' measurements to understand the differences between atomic and molecular ion responses, a natural consequence for which the algorithms cannot anticipate or compensate.

2.2.1. TOF Differences

For ions with the same total mass and incident energy per charge MI TOFs are measurably longer than atomic ion TOFs. Molecular ions are known to lose energy in solids in a more complicated manner than atomic ions (see, e.g., Tape et al., 1976, Note 21 of Geiss et al., 1992, and the discussion in the SI for Christon, Hamilton, DiFabio, et al., 2013). Depending on an MI's internal structure, speed, and alignment/orientation with respect to its velocity vector, a diatomic ion, N_2^+, for example, can lose more or (rarely) less energy than two independent N^+ ions entering the material simultaneously at the same initial velocity (see, e.g., Heredia-Avalos & Garcia-Molina, 2007; Eckardt et al., 1978; Song et al., 2005, and references therein). In the rare instance where a MI's axis of symmetry is aligned along its direction of motion, it can lose less energy than when its axis is otherwise oriented, or when its component ions travel independently at the same velocity for the same distance in the medium (see Figure 5 of Arista, 2000). Generally though, in a randomly oriented distribution, more typical in nature, where only a small fraction of molecular orientations are parallel to the general direction of ion travel, molecular ions will generally lose more energy on the average than the independent, identical, constituent, elemental/atomic ions of the molecule, or the rare parallel-alignment ions. This additional energy loss results in a lower particle kinetic energy upon exiting the foil and a longer subsequent TOF. This longer TOF results in a higher resultant calculated M/Q value for molecular ions than for atomic ions with the same mass. In a later section we demonstrate the measured difference between molecular ion TOFs to atomic ion TOFs for several selected energy channels.

2.2.2. Measured Residual Energy Deposit (Em) Differences

There are major, observable differences between atomic and molecular ion energy deposits in the SSD. First, MI dissociation and scattering in the carbon foil results in a bimodal set of energy deposits (Em) for MI. One mode represents the small scattering situation in which both constituent ions deposit energy in the SSD. The other mode occurs when only one constituent atom deposits its energy in the SSD and the other atom scatters out of the flight path. Consequently, MI data generally result in bimodal mass distributions as is shown below. After DPU-based corrections for detection phenomena, such as the well-known pulse-height defect (Campbell & Lin, 1973; Ipavich et al., 1978), MIs register higher than anticipated calculated masses in these instruments compared to atomic ions of equal incident energy. On the spacecraft, the DPU assigns and classifies each ion according to fast mass-per-charge and mass on board encoded algorithmic calculations. An ion's mass determination is positively correlated with both the (1) time of flight and (2) energy deposited in the solid-state detector. The energy measured by a stopping ion is typically less than the ion's incident energy, and this deficit in measured energy increases with the mass of the incident ion (Ipavich et al., 1978). The DPU's mass calculation assumes atomic ions, the most typical situation in space particle populations, and this assumption results in an overestimate of an MI's mass assuming that both constituent atoms hit the SSD. For an illustrative example with supporting calculations, see Figure S4 in the SI, which compares Ar^+ and the noble-gas dimer $Ne_2{}^+$, which both have a total mass of ~40 amu. The DPU algorithm's mass correction, which uses the MI's mass determined from the M/Q measurement presuming an incident singly charged single-nucleus atom, is applied to the two constituent atomic ions, each with approximately one half of the MI's total mass. As a result of the mass-deficit feature, the constituent ions together deposit more energy than an ion with a mass equal to the sum of the MI's atomic constituents. Assuming an atomic ion, the DPU overcorrects the already higher-energy deposit (from each of two atoms) with the higher value related to the heavier atomic ion's (presumed smaller) mass deficit, resulting in a higher than nominal mass calculation for the MI. The instrument's default calculation clearly overestimates the total mass for MI, which deposit a maximum energy from both constituent atoms in the nonscattering condition.

The above differences between atomic and molecular ions' M and M/Q distributions both enable and are essential in, the separation of the ionospheric molecular ions, $N_2{}^+$, from lunar atomic ions, Si^+, near Earth. In the near-Earth solar wind Mass-30 ions have a significant lunar PUI signal of varying proportion depending on the plasma regime of observation. Earth's SW/IM MI data are the most strongly affected, with the PUI most apparent when the Moon is sunward of Earth during high geomagnetic activity intervals, which result from high-speed solar wind flow.

2.2.3. $^{A}Mq^+$, $^{A}Ma^+$, and $^{A}M^+$ Naming Conventions

Using the atomic ions at Earth, Jupiter, and Saturn from our analyses, the M/Q values of atomic ions have been adjusted slightly, for example, correcting for slight differences in the various instruments resulting from algorithmic approximations and possible foil thickness variations, so that their M/Q response peaks are centered closer to their nominal masses (Christon, Hamilton, DiFabio, et al., 2013, Christon et al., 2017). We therefore expect singly charged heavy atomic ions to be rather close to their nominal mass per charge values. MI species register slightly higher M/Q values than the sum of their component atomic ions, possibly on account of their lower than atomic ion's TOF velocity resulting from the MI's stronger interaction with and subsequent higher-energy loss in the instrument's carbon foil. For initial species identification, we, as does the instrument's electronics, rely on the higher-resolution M/Q-resolved, rather than the much lower resolution M-resolved, species determination. Please note that when we feel it necessary in this paper, we utilize generic, analysis-specific naming conventions for clarity: When addressing data and the method of collection is important, we use $^{A}Mq^+$ and $^{A}Ma^+$, where A is the mass of the ion and Mq (Ma) indicates that the data are ordered by and binned along the M/Q (M) axis, accumulating over the other variable M (M/Q). Depending on the context of usage, the identity of the ions is either known, unknown, generalized, presumed, or indeterminate because there may be two or more known or presumed individual ion species in the mass-variable range, irrespective of the mass-based variable. The form $^{A}Mq^+$ ($^{A}Ma^+$) applies to ions identified through and ordered by M/Q (M), categorization and classification, typically in discussions of data collection, and analysis. Ions in the generic ranges ~12–19, ~20–26, ~27–33, and ~39–48 are generically called Mass-16, Mass-20, Mass-30, and Mass-40 ions. If the method of ordering is not relevant in a discussion, we simply refer to $^{A}M^+$ ions, such as "Mass-30 ions" are identified as $^{30}M^+$ ions. At times, we use histograms of PHA data ordered by either M/Q or M, sometimes with a range criterion placed on the other variable, M or

M/Q, respectively. Ordering by M/Q (^{A}Mq^{+}) is more often than not utilized for accumulations over the full range of M values. On the other hand, ordering by M (^{A}Ma^{+}) is most likely presented for accumulations over a wide range of Mass values and a limited range of M/Q values. Both conventions are used as needed in the analysis.

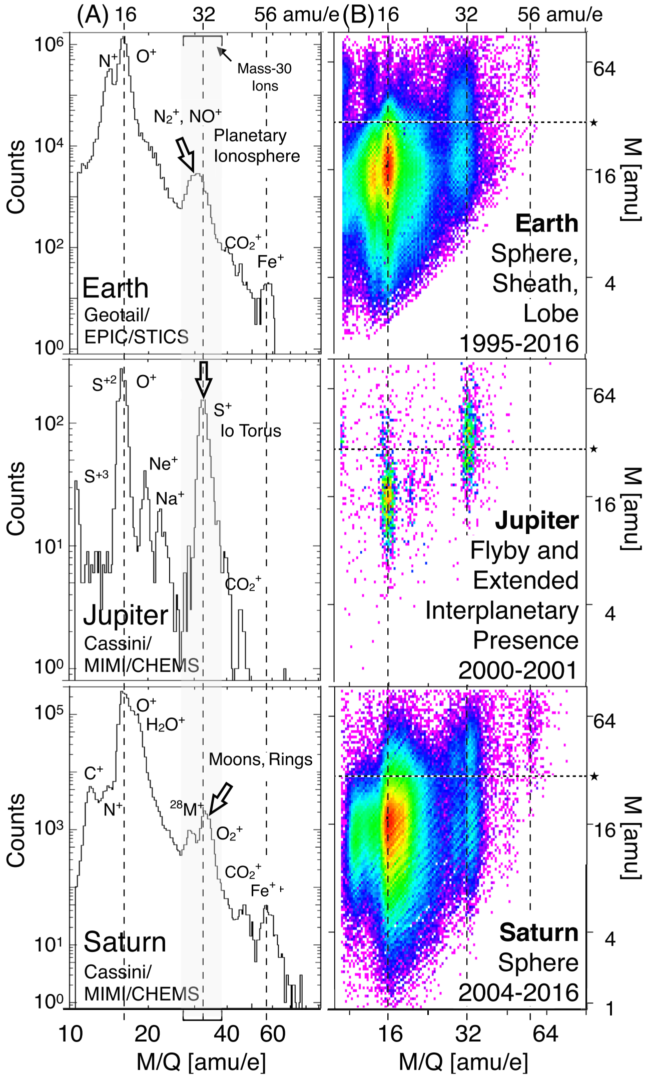

Figure 1. Heavy suprathermal (CHEMS, ~83–167 keV/e; STICS, ~87–212 keV/e) ion Pulse Height Analysis PHA data obtained by (top) Geotail in and near Earth's magnetosphere; (middle) Cassini during its Jupiter flyby and in the interplanetary medium from ~3 to 9 AU when S^+ was measured; and (bottom) Cassini in Saturn's $\lesssim$20 Rs magnetosphere (see text for details). The PHA data are presented as (a, left) mass-per-charge (M/Q) histograms and (b, right) mass (M) versus M/Q color spectrograms (color bars suppressed). Stars at right and horizontal dashed lines identify M = 32 amu. All data were adjusted slightly in order to center N^+, O^+, and S^+ on their atomic mass in order to account for instrument and spacecraft electronics differences. Mass-30 ions include ~27–33 amu/e. General sources of the Mass-30 ions at each planet are noted.

3. Observations

Figure 1 summarizes major similarities and differences in the three planets' magnetospheric heavy ion composition, with a specific focus on the clear differences between Mass-30 ions (~27–33 amu/e), observed at the three planets, although aspects of the Mass-40 ions (~39–48 amu/e) are important at Earth. The high-resolution M/Q measurements are a more accurate and precise tool with which to collect, order, and separate ion species than the lower resolution M measurements. However, the information conveyed by the M-M/Q color spectrograms is critical for clearly identifying and separating different atomic and molecular ion charge-state species having similar M/Q values. Vertical dashed lines are drawn at 16, 32, and 56 amu/e to simplify data set comparisons and demonstrate the level of accuracy and possible precision of our procedures. The M/Q comparison is accurate enough to demonstrate that the three Mass-30 populations are uniquely different: ^{28}Mq^{+} and ^{30}Mq^{+} ions at Earth; S^+ dominating at Jupiter; and ^{28}Mq^{+} and ^{32}Mq^{+} ions at Saturn. Fe^+, at ~56 amu/e, is observed at Earth and Saturn, but not at Jupiter or in the interplanetary medium (as shown below). Please note that the generic ion identifier Mq was introduced in the final paragraph of section 2.2.

In our long-term averages in Figure 1, O^+ is the principal magnetospheric suprathermal heavy ion at all three planets, but not necessarily dominant at all times; levels of H_2O^+ and S^+ comparable to O^+ exist at Saturn and Jupiter, respectively, and the seasonal variation of O^+ at Earth results in N^+/O^+ ~1 during solar minimum (Christon et al., 2002; Mall et al., 2002). Additionally, solar wind plasma clearly enters planetary magnetospheres and is subsequently incorporated into their magnetospheric ion populations (Christon, Hamilton, et al., 1994; Mitchell et al., 2018; DiFabio, 2012; Peterson et al., 1998; Spjeldvik & Rothwell, 1985; Pan, 2015), although solar wind contributions to magnetospheric populations vary by planet and solar season (e.g., DiFabio et al., 2011; Fujimoto et al., 1996, 1998; Peterson et al., 1981; Terasawa et al., 1997). As a result of this, the proportion of solar wind pickup O^+ (and/or lunar-origin pickup O^+ in the case of Earth) entering a magnetosphere to the O^+ generated internally, escaping, and possibly reentering at any of the magnetospheres (see, e.g., Cohen et al., 2016; Sorathia et al., 2017) is not estimable from single-spacecraft studies such as this. Likewise, O^+ escaping from a magnetosphere may not be separable from interplanetary pickup O^+, even using full three-dimensional distribution functions. At Jupiter, the presence of S^{+2} at ~16 amu/e in Figure 1b, middle panel signals that both S and O are important suprathermal ions at Jupiter and dominance by one or the other, may vary depending on the energy range (see, e.g., Haggerty et al., 2009). Regardless, in the central magnetotail plasma sheet and dayside equatorial regions of each magnetosphere, O^+ is likely often the dominant heavy ion at all three planets. At Jupiter, O^+, S^+, and Na^+ originate mostly from Io; although icy Galilean satellite data show the presence of O_2, their O_2 is not presumed to necessarily escape the satellites (Johnson et al., 2004). Figure 1 shows that we observe peak $O^+/S^+ < 2$ at Jupiter, while at Earth O^+/N^+ is ~5, and at Saturn O^+/H_2O^+ is ~2–3. Please note that the ions in the prominent O^+-H_2O^+ peak at Saturn are often referred to as the water group ions, or W^+. W^+ ions

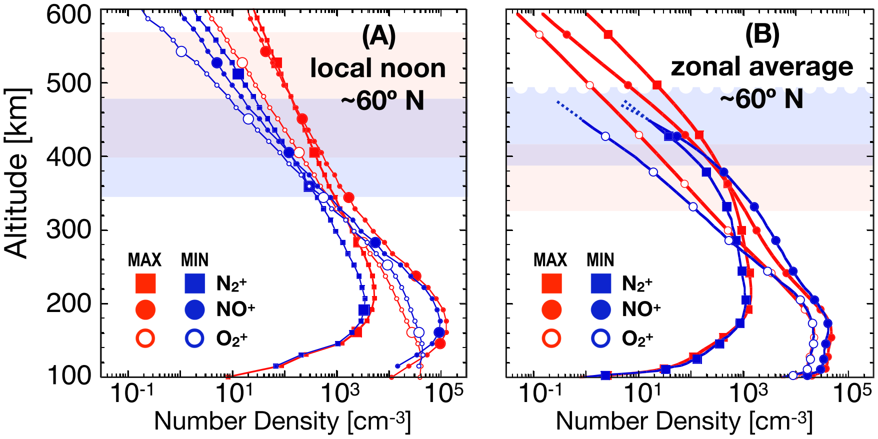

Figure 2. Earth's dayside molecular ion number density profiles of N_2^+, NO^+, and O_2^+ at ~60°N latitude around Spring equinox calculated for solar maximum (MAX) and minimum (MIN) conditions from (a) the SAMI3 ionosphere model near local noon and (b) the WACCM-X thermosphere/ionosphere model for a one-month narrow-latitude zonal average; see text for input parameter and run information. Unique symbols identify and differentiate the three MI species' altitude profile similarities and differences. The red and blue shaded areas indicate altitude ranges that vary with solar cycle in which the N_2^+, NO^+ densities are approximately equal and O_2^+ levels are somewhat lower, but not absent. This unique molecular ion composition signature is characteristic of outflowing MI (see text).

contain O^+, OH^+, H_2O^+, and H_3O^+ (see, e.g., DiFabio et al., 2011, Allen et al., 2018; Martens et al., 2008). Molecular and atomic ions from the satellites and rings of Jupiter and Saturn are likely the primary sources of their planet's magnetospheric O^+ populations, while, on the other hand, Earth's ionosphere, not the Moon or interplanetary sources, is the source of most of Earth's magnetospheric O^+. The Ne^+ identified near Jupiter in Figure 1 is an interstellar pickup ion (Gloeckler, Fisk, Geiss, et al., 2000; Gloeckler, Fisk, Zurbuchen, & Schwadron, 2000).

Heavy open arrows in the Figure 1 histograms indicate significant differences in the M/Q distribution of Mass-30 ions at the three planets. Mass-30 ions are a small percentage of O^+ at Earth and Saturn, but comparable to O^+ at Jupiter. Inside Earth's bow shock, Mass-30 ions have a broad, rounded peak centered primarily below 32 amu/e suggesting outright, without any further information, that they are probably dominated by N_2^+ and NO^+, but are clearly missing a coequal O_2^+ component, which would have resulted in a peak level extended to and above ~32 amu/e. At Jupiter, the atomic ion S^+ is the dominant Mass-30 ion, its peak centered on 32 amu/e. At Saturn, the well-documented and well-understood O_2^+ magnetospheric Mass-30 MI peak is clearly centered at M/Q >32 amu/e, consistent with our current new understanding of the instruments presented in section 2. The question remains as to how much O_2^+ is present in Earth's magnetosphere.

We briefly present calculations from two recent ionospheric models showing that less O_2^+ than either N_2^+ or NO^+ is expected to flow out of the ionosphere for outflow initiated at altitudes of ~250–500 km, consistent with the cited ionospheric studies and our MI observations in Earth's magnetosphere. Large local time variation of ionospheric density, being about 2 orders of magnitude higher on the dayside than on the nightside (see, e.g., Yau et al., 1993), focuses interest on dayside outflow. Solar cycle variation of dayside ionospheric densities is demonstrated in Figure 2 using ion number density results from two recent ionospheric models, WACCM-X (Liu et al., 2010, 2018) and SAMI3 (Huba et al., 2000, 2008). Both are three-dimensional models of Earth's ionosphere and thermosphere, which predict ion profiles that are generally similar to the in situ ionospheric observations of Yau et al. (1993), Peterson et al. (1994), and Foss et al. (2017). Recent observations (e.g., Andersson et al., 2004; André & Cully, 2012; Haaland et al., 2012; Wilson et al., 2004; Yu & Ridley, 2013) collectively demonstrate that both the dayside cusp and the nightside auroral zone can contribute substantial quantities of outflowing ions (from cold, ~eV, to tens of eV energies) to the total ion plasma population throughout the magnetosphere, as well as to the many energized ionospheric origin ions that are quickly lost downtail (see, e.g., Christon, Gloeckler, et al., 1994). André and Cully (2012) state that although the outflowing polar wind mostly flows into the tail, some tens of percent of low-energy polar wind flow are diverted through the dayside magnetopause for southward IMF. Figure 2 concisely summarizes model number densities of N_2^+, NO^+, and O_2^+ in Earth's high-latitude ionospheric source regions for solar maximum and solar minimum conditions. The model time selections for Figures 2a and 2b are different: In Figure 2a with SAMI3 we calculate 2-day averages for two widely different sets of conditions: First, quiet geomagnetic activity during low solar activity and second disturbed geomagnetic activity during high solar activity; in Figure 2b, monthly zonal averages around times of solar maximum and minimum are calculated. Calculations in Figure 2b from SAMI3 (at https://ccmc.gsfc.nasa.gov/models/modelinfo.php?model=SAMI3) and WACCM-X (at https://www2.hao.ucar.edu/modeling/waccm-x) show that although O_2^+ can contribute significantly between ~100 and 150 km, it becomes a minor component at altitudes higher than ~300–450 km and latitudes ≥50°, locations where ionospheric outflow ion composition is determined. Model outflow from these higher regions shown in panels 2a and 2b results in outflowing MI dominated by nearly equal parts of N_2^+ and NO^+, each generally more populous than O_2^+ by a factor of >3, irrespective of solar and geomagnetic activity (see Table S10 in the SI for the SAMI3 and WACCM-X model run parameters and intervals). That $O_2^+/(N_2^+ + NO^+) < 1$, characteristic of the ionospheric observations noted above, is shown by several other ionospheric models (Köhnlein, 1989; Cannata, 1990; Richards, 2013; see also Hoegy et al., 1991). We note further that in an investigation demonstrating solar cycle variation of ionospheric MI by Richards (2013), who used yet a different model, O_2^+ was shown to decrease relative to N_2^+ and NO^+ above ~280–290 km. Results from these various models are generally consistent, but the public access to WACCM-X and SAMI3 allows interested readers to look further into the MI compositional aspects demonstrated here. We now resume our investigation of the new information in this report, which will reveal that throughout the equatorial $\sim 9 < R < \sim 30$ Re magnetosphere, outflowing ionospheric N_2^+ and NO^+ quantities are comparable, and a relatively smaller amount of O_2^+ escapes overall.

Differences between atomic and molecular ion responses are immediately apparent in the instruments' color spectrograms in Figure 1b, where atomic ions at all three planets, such as N^+, O^+, S^+, and Fe^+, exhibit single-peaked Mass distributions, but the Mass-30 MIs, N_2^+ and NO^+ at Earth and $^{28}M^+$ and O_2^+ at Saturn, exhibit two Mass peaks as discussed in section 2.2. No apparent MI instrument responses are clearly evident at Jupiter. Horizontal white, dashed reference lines drawn at $M = 32$ amu in the color spectrograms (note the stars to the right of the right-hand panels) show that the upper MI peaks are located at Mass values displaced ~25–40% higher than the incident ion's mass, $M \sim 28–32$ amu. This overestimation of a MI's total Mass, discussed in section 2, is visible in Figure 1b at Earth and Saturn for each of the Mass-30 MI distributions. Although the Mass axis is only roughly calibrated, note that Jupiter's S^+ Mass distribution is centered at ~32 amu (midway between 16 and 64 amu on the log scale axis) and the O^+ distributions at all three planets peak at ~16 amu.

3.1. Jupiter

In Jupiter's magnetosphere, where we obtained the least information, we primarily address S^+, our Mass-30 atomic ion M/Q reference fiducial. Jupiter's high-energy particle radiation environment appears to quickly dissociate and ionize most, if not all, molecules into their component atomic ions. These molecules may include SO, SO_2, and S_2 anticipated from Io (Wilson et al., 2002), CO, CO_2, H_2O, and O_2 from Ganymede, Europa, and Callisto (e.g., Carlson, 1999; Cooper et al., 2001), or Jupiter family comets (Bockelée-Morvan, 2011), and/or NaCl and/or NaOH from Io (Kuppers & Schneider, 2000; McEwen et al., 2007). Io's molecules result in predominantly S^+ and O^+ at suprathermal energies, as evidenced in Figure 3. We do not observe a peak near the expected locations of SO_2^+ and S_2^+ at $M/Q \gtrsim 64$ amu/e in or near Jupiter's magnetosphere, suggesting that all ionian SO_2^+ and S_2^+ quickly dissociate before they can be accelerated to suprathermal energies or that our detection efficiency for the very heavy ions is too low. We presume that a large amount of asteroid belt material in the form of interplanetary dust particles, or IDPs, are also drawn into and present in Jupiter's intense magnetospheric radiation environment. Although we would anticipate all MI to dissociate in Jupiter's magnetosphere, the suggestive, but small, signals at ~45 amu/e in and near Jupiter's magnetosphere presents a conundrum. The possible species that could result in an ~44–46 amu/e signal are Sc^+ (with Mass of 45 amu), SiO^+ (44 amu), CO_2^+ (44 amu), and/or possibly $SiOH^+$ (45 amu). The abundance of Sc in cosmic dust, the most likely Sc source at Jupiter, is small, but Si compounds are prevalent in IDPs (Grebowsky & Aikin, 2002; Plane et al., 2016). However, most, if not all, IDP material likely dissociates completely into its component atoms at Jupiter and we assume it unlikely that any IDP origin MIs survive and

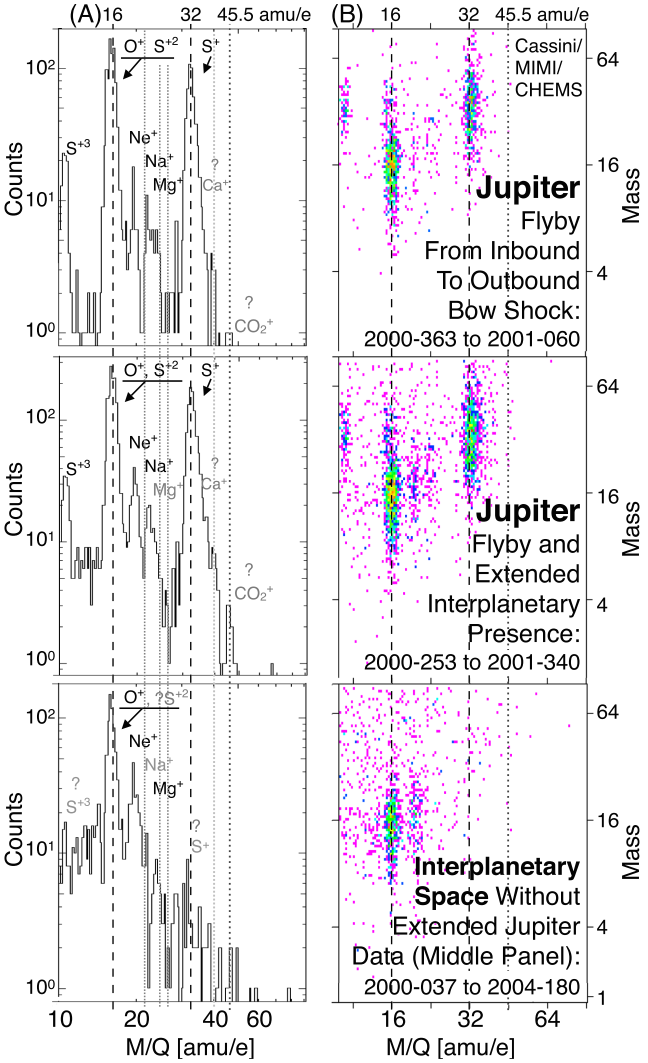

Figure 3. Cassini's measurements of Jovian and solar wind/interplanetary medium suprathermal (~83–167 keV/e) ion populations during: (top) the Jupiter flyby between inbound and outbound bow shock encounters; (middle) the extended interval over which S^+ from Jupiter was detected in the solar wind before, during, and after the Jupiter flyby; and (bottom) the ~3-year Cassini cruise to Saturn, excluding the extended ~1-year interval of Jovian fluxes from the middle panel. The tentative identification of Jovian magnetospheric Ca^+ and CO_2^+ are noted by lighter dotted lines.

are observed in Jupiter's magnetosphere. Therefore, assuming that this is likely an MI signal and remembering that MI energy loss in the carbon foil results in a higher than expected M/Q value for MIs than atomic ions, the remaining 44-amu MI candidate (with an ~45 amu/e M/Q value) is CO_2^+. Therefore, this small, distinct peak may be evidence of CO_2^+ derived from Jupiter's Galilean moons (Gomis & Strazzulla, 2005; Hibbitts et al., 2000) or Jupiter family comets (Bockelée-Morvan, 2011). Ne^+, Mg^+, and some O^+ are interplanetary pickup ions (Kallenbach et al., 2000) as the interplanetary data in the bottom panels suggest, although magnetospheric Mg^+ might also derive from outflowing IDP material ablated in the ionosphere of Jupiter (Kim et al., 2001) and/or possibly that of Ganymede, whose diameter at ~0.4 times that of Earth, from which it would be easier to escape. (However, the lack of observed Fe^+ near Jupiter makes an IDP source seem less likely.) Jupiter's magnetospheric Na^+, O^+, and S^+ likely derive from Io (Bodisch et al., 2017; Wilson et al., 2002), while the other icy Galilean moons may also contribute to O^+ (Strobel & Yung, 1979). Jupiter's primary contribution to this study is the strong, clear S^+ atomic-ion distribution at 32 amu/e, which we use as our Mass-30 M/Q reference fiducial. S^+ became increasingly discernible after day 2000-253, ~0.7 AU from Jupiter (Krimigis et al., 2002). S^+ remained intermittently present out to ~6.6 AU and was not detected after days 325–340, 2001 (see Figure 3 and Table S2 in the SI). Note also that (a) S^{+2} and S^{+3} components, centered at ~32 amu and ~10–11 and ~16 amu/e, respectively, are evident in the upper and middle M-M/Q color spectrograms, where the S^{+2} would otherwise be masked by O^+ if only M/Q measurements without the accompanying Mass measurements were available; and (b) the S^+, $O^+(S^{+2})$, and S^{+3} count levels in the middle histogram (flyby and extended interplanetary S+ presence) are each higher in the middle histogram than their respective peaks in the top histogram (flyby from inbound to outbound bow shock). Comparison of the top histogram to the middle histogram shows that each of these groups, the S^+, $O^+(S^{+2})$, and S^{+3}, escapes Jupiter and is present in interplanetary space outside the bow shock. Although not shown herein, we found that all of the S^{+3} in the extended interplanetary S^+ data in Figure 3's middle panel is measured tailward of Jupiter, none was measured sunward of Jupiter. In the lower histogram, a trace ion signal at ~39–40 amu/e present in and near Jupiter's magnetosphere (3a and 3b), but not in interplanetary space (3c), may represent $^{39}K^+||^{40}Ar^+||^{40}Ca^+$ (please note that we use the logical symbol "||" below to represent the phrase "and/or" when there are two or more candidate ions that cannot be differentiated). Only $^{33/38}Ar$ and CO_2 have currently been identified in Jupiter's atmosphere (Kunde et al., 2004; Mahaffy et al., 2000). However, although cosmic dust and Jupiter Family comets possibly containing K, Ca, SiO, and CO_2 likely interact with Jupiter's magnetosphere, we will restrict our discussions/references of Jovian Mass-40 ions to Ca^+ and CO_2^+.

3.2. MI at Saturn and Earth

Mass-30 ion data obtained at Saturn from late 2004 to late 2007 are plotted vertically in Figures 4a and 4b for ease of comparison: (4a) inside Saturn's magnetosphere at ~4 < R < 20 R_S, in the Sphere (Christon, Hamilton, DiFabio, et al., 2013, Christon et al., 2014, 2015) and (4b) in the solar wind outside Saturn's magnetosphere at $R > R_{BS}$ (the Saturn bow shock distance). Cassini magnetopause and bow shock crossings were determined by a Cassini magnetosphere and plasma science research team for the years 2004–2007. Lists of the intervals collected for this study are in the SI. Note that we refer to Saturn's $R < 20$ Rs and $R > R_{BS}$ data as Saturn's "Sphere" and "Solar Wind" data, respectively. The top panel of Figure 4 shows that Earth's Mass-30

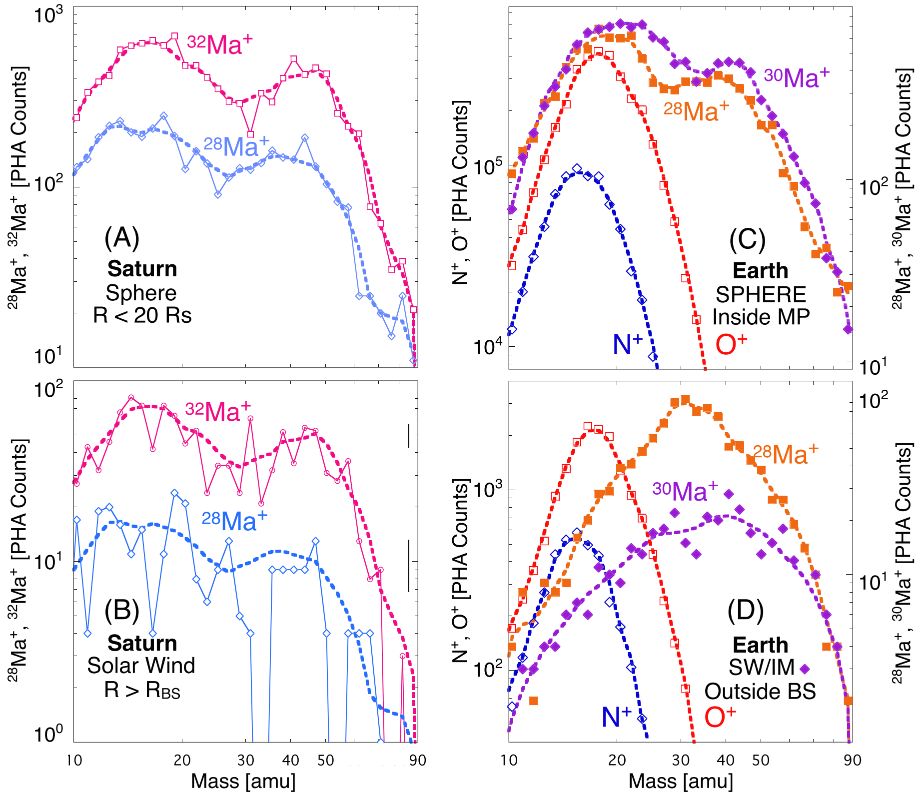

Figure 4. Mass distributions of Mass-30 suprathermal (CHEMS at Saturn, ~83–167 keV/e; STICS at Earth, ~87–212 keV/e) ion data at Saturn and Earth highlight atomic and molecular ion (MI) differences. Data points and smoothed fits are shown. The indeterminate species descriptors "$^{28}Ma^+$" and "$^{30}Ma^+$" are used as ion species channel names in this figure for primarily singly charged Mass-30 ions selected in narrow M/Q ranges near 28 and 30 amu/e because it is clear that there is an admixture of ion species in at least two cases. The identifier "Ma" represents a M-M/Q spectrogram selection over a limited M/Q, but wide M, range in which the selected ions' species identification is sometimes complex (see text for the full discussion). Mass histograms of $^{28}Ma^+$, $^{30}Ma^+$, and/or $^{32}Ma^+$, heavy ion species having mass numbers of 28, 30, and 32 amu, respectively, are likely dominated by one or a combination of the ions identified as $^{28}M^+$ (CO^+, N_2^+, $HCNH^+$, and/or $C_2H_4^+$ at Saturn and N_2^+ at Earth), NO^+, and O_2^+. At Saturn, data from mid-2004 through 2007 containing: (a) All intervals when Cassini was in Saturn's magnetosphere, the Sphere, at ~$4 < R < 20$ R_S and (b) only intervals in the solar wind for which an outbound and a subsequent inbound bow shock (BS) crossing were identified, including travel to and from apoapsis, thus placing Cassini in the Solar Wind near Saturn at $R > R_{BS}$, the distance of Cassini's bow shock encounters. Representative uncertainties are shown near the right vertical axis in (b). At Earth, data from early 1995 through 2015 are shown for intervals when Geotail was in (c) the SPHERE, Earth's magnetosphere, and (d) the SW/IM, the near Earth, unshocked, solar wind of the interplanetary medium. See text for details.

molecular ion mass distributions, $^{28}Ma^+$ and $^{30}Ma^+$, overlap significantly. Therefore, the observationally determined distributions in M we show in Figure 4 and discuss below are collected in narrow M/Q range selections near the center of their M/Q distributions in order to limit background spillover from nearby species. Spillover from $^{30}Ma^+$ ions into $^{28}Ma^+$ ions is unlikely, as TOF variations are physically limited toward longer TOFs. The curves for $R < 20$ Rs are smoothed fits to the PHA histogram. As a result of the uncertainties associated with defining a best fit to the low counting statistics of the $R > R_{BS}$ data, we simply redrew the fitting curves from $R < 20$ Rs at appropriate levels for the $R > R_{BS}$ data in order to highlight these ions' apparently consistent spectral shape similarity inside and outside Saturn's magnetosphere. For clarity, representative count uncertainties are only shown at two values near the right-hand axis in Figure 4b. No atomic ions appear to be present in these $^{28}Ma^+$ and $^{32}Ma^+$ data collections either inside or outside Saturn's magnetosphere, only molecular ions. The $^{28}Ma^+$ (light blue) and $^{32}Ma^+$ (rose) Mass-30 ions likely dominated by one or several of the aforementioned $^{28}M^+$ ions and O_2^+, respectively, are more widely separated, so there is somewhat less spillover at Saturn (see Figure S8 in the SI). While the species identification of O_2^+ at $^{32}Ma^+$ is much more certain than that of $^{28}Ma^+$

(Christon, Hamilton, DiFabio, et al., 2013; Christon et al., 2015), noncommittal species descriptors are used for all molecular ion species in this figure. Both MI species at Saturn display a clear two-lobed shape in the magnetosphere and, most likely, in the solar wind, although the statistics are poorer there than in the magnetosphere. The bimodal MI shapes at Saturn are consistent with those observed in Earth's magnetosphere (panel 4c), which suggests measurements of predominantly diatomic Mass-30 MI (see section 2) inside both magnetospheres. Figures 4a and 4c demonstrate that there is no significant difference in instrument response characteristics to MI inside the two planets' magnetospheres and that other than two MI species, we do not detect any evidence for Mass-30 lunar PUI (Al^+, Si^+, or P^+) at measurable levels in Earth's SPHERE plasma regime. Future selective analysis might help reveal times when the atomic lunar PUI in this Mass range are visible in the SPHERE, but that is not our current objective.

Figures 4c and 4d show the Mass-30 ion mass distributions from Earth's magnetosphere, SPHERE, and the near-Earth solar wind, SW/IM, respectively. The shapes of the Mass-30 ions, $^{28}Ma^+$ (orange) and $^{30}Ma^+$ (purple), compared to those of the dominant atomic ions O^+ (red) and N^+ (blue) at Earth and to the MI data at Saturn in Figures 4a and 4b, indicate that Earth's SPHERE data in Figure 4c contain clear MI responses similar to those from Saturn' Sphere. However, Earth's SW/IM Mass-30 channels in Figure 4d do not contain clear MI responses. Review of Figure 2 suggests that there is no detectible spillover of O^+ into the MI distributions at either planet. Unlike the situation at Saturn, where Sphere and Solar Wind shapes are nominally similar, the shapes of Earth's SW/IM $^{28}Ma^+$ and $^{30}Ma^+$ distributions are not similar to the shapes of either Saturn's or Earth's magnetospheric MI distributions or any single atomic ion's distribution. The less sharply peaked $^{30}Ma^+$ SW/IM distribution's shape is only slightly more similar to the MI shapes in the SPHERE than to the shape of the SW/IM $^{28}Ma^+$. As an operating presumption, we demonstrate below that the difference between Earth's SPHERE and SW/IM Mass-30 ion distributions indicates the presence of lunar PUI responses in Earth's $^{28}Ma^+$ and $^{30}Ma^+$ SW/IM data. Relative mixtures of PUI and ionospheric contributions present in the two ion channels are not the same. Different portions of the three lunar PUIs' Mass distributions contribute to the two channels, specifically, Al^+ and Si^+ in $^{28}Ma^+$, and Si^+ and P^+ in $^{30}Ma^+$, consistent with earlier lunar PUI composition measurements. We now briefly discuss relevant aspects of Mass-30 ion comparisons at Earth and Saturn to clarify the effects of the lunar PUI background interference on our MI observations.

Figure 5 compares long-term average heavy ion composition measurements normalized to O^+ in the near-Earth and near-Saturn plasma regimes. Histograms of magnetospheric data are shown in red (measured using red axis values on the left), contrasted with magnetosheath and/or solar wind data in blue (measured using blue axis values on the right). As noted above, the plasma regime label terminologies for Earth and Saturn data are individualized, constructed to be uniquely different visually, so that textual references to each planet's plasma regimes should not to be mistaken for the other's and the reader can clearly and easily differentiate between the two planets in our discussions and comparisons. The labeling differences also highlight the different plasma regime identification procedures at the two planets (see section 2 and Christon, Hamilton, DiFabio, et al., 2013, Christon et al., 2017). Shown are ~21 years of data at Earth and ~3 years at Saturn, so that vertical scaling is consequently different for the two planet's panels. However, vertical scaling for each panel's right and left axes is identical, with the deficit on the right-hand axes left open to highlight intensity differences. Dashed fiducial lines at 16, 32, and 56 amu/e are drawn to simplify comparisons (color spectrograms for these Earth and Saturn data are in Figure S3, and nominally drawn, unnormalized individual panels are in Figure S13 in the SI). Despite the vast difference in the Earth and Saturn magnetospheric sizes, the ratios of Mass-16 atomic ion levels in the two magnetospheres compared to their levels in the planets' nearby sheath and solar wind are very similar as shown in Figures 5b and 5c; that is, at Earth, the ratios $N^+/O^+_{\mathrm{SPHERE}} \approx N^+/O^+_{\mathrm{SHEATH}} \approx N^+/O^+_{\mathrm{SW/IM}}$, and at Saturn, $N^+/O^+_{\mathrm{Sphere}} \approx N^+/O^+_{\mathrm{SolarWind}}$ and $C^+/O^+_{\mathrm{Sphere}} \approx C^+/O^+_{\mathrm{SolarWind}}$. Saturn's Sheath data are excluded for brevity. Of note, H_2O^+ is the only ion in these comparisons whose PHA counts relative to O^+ can be seen to decrease significantly outside the magnetosphere rather than increase (this also likely occurs for OH^+, but OH^+ is masked by O^+ and H_2O^+). The Mass-30 data at Saturn are most informative because the escape of its MI into the Solar Wind appears to be uncomplicated (as shown above in Figures 4a and 4b), in that the escaped MI measurements in the Solar Wind are not masked by other Mass-30 ion species; the same MI species measured in the Sphere are those measured in the Solar Wind

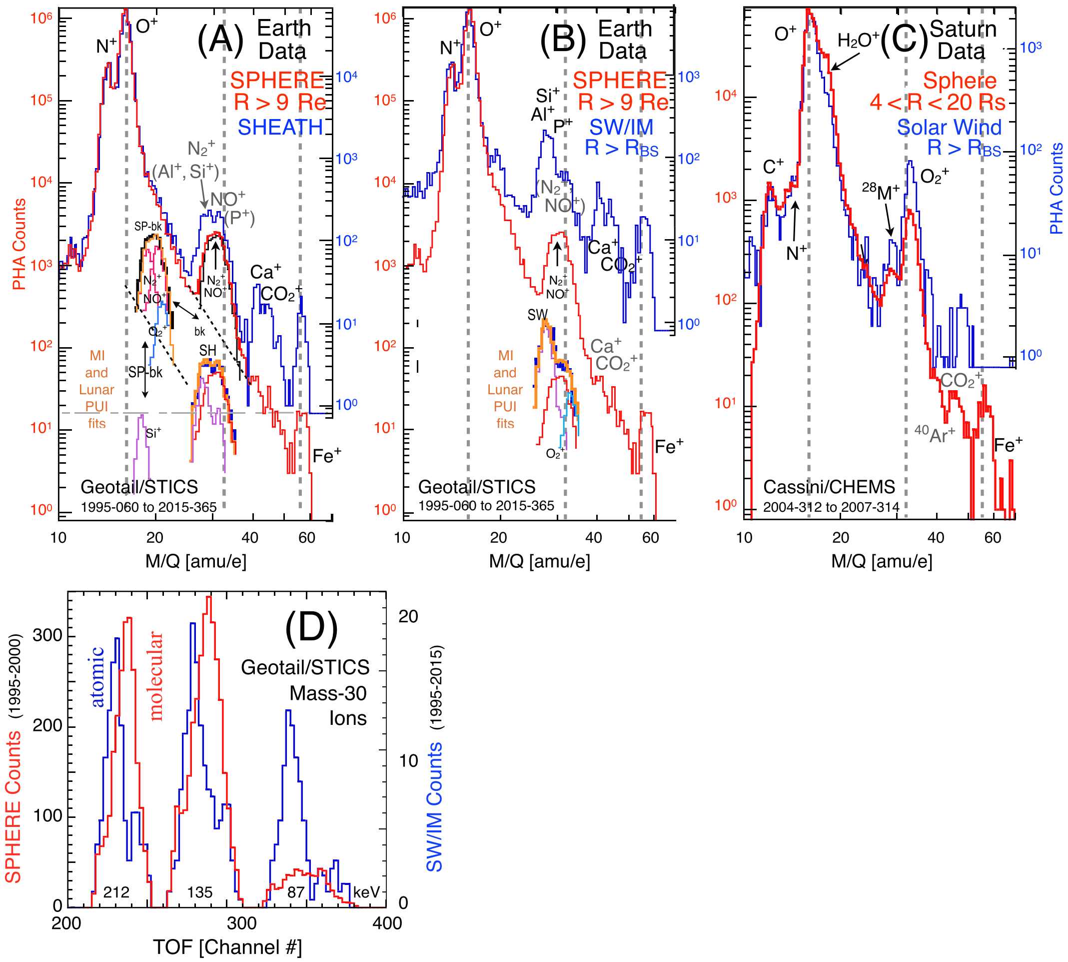

Figure 5. Long-term suprathermal (CHEMS, ~83-167 keV/e; STICS, ~87–212 keV/e) heavy ion composition measurements in near-Earth (A, B) and near-Saturn (C) plasma regimes are normalized to O^+ and compared directly. The vertical axes of SPHERE data (red left axis labels), SHEATH, and SW/IM data (blue right axis labels) are offset in order to compare selected species' importance relative to O^+. Shown are ~21 continuous years of Earth data and samples from ~3 years of select Solar Wind and contemporaneous Sphere intervals at Saturn. Note the distinct plasma regime labeling which differentiates the two planets' regimes in the text and highlights their different selection procedures. Vertical fiducial lines at 16, 32, and 56 amu/e are drawn to simplify visual comparison. At Earth, the Mass-30 SHEATH (A: blue) distribution is intermediate between that of the SPHERE (A, B: red) and SW/IM (B: blue). Floating insets (near bottom of A and B) show rough visual fits (orange) to the background (bk) subtracted SPHERE (SP-bk, black), SHEATH (SH), and SW/IM (SW, at distances $R > R_{BS}$, the distance to the bow shock) data. The fits use SPHERE MI (A: rose for N_2^+ and NO^+, light blue for O_2^+) and select distributions of lunar pickup ions, PUI, and/or, in the case of the SPHERE, ionospheric Si^+ (purple) at the Fe^+ level (long-dash line). Prominent lunar PUI species are identified. (D) In these instruments, dominant SPHERE molecular ion (MI) dissociation energy loss in the carbon foil result in slightly longer times-of-flight (TOF) with subsequently higher M/Q values than for the dominant SW/IM atomic ions of the same mass. See text.

outside Saturn's bow shock. Mass-30 MIs are dominated by equal amounts of N_2^+ and NO^+ in Earth's magnetosphere and primarily by O_2^+ at Saturn, except at equinox (Christon, Hamilton, DiFabio, et al., 2013), with overall average MI/O^+ ~0.1% at each. That normalization to O^+ does not introduce uncertainty in this presentation of the relative importance of escaped magnetospheric ions and lunar PUIs is supported by the similarity of Mass-16 atomic ions' relative intensities inside and outside these two magnetospheres noted above. (Interested readers can find Figure 5 data plotted separately with identical vertical axes in Figure S13 in the SI.) This similarity suggests that the magnetospheric and solar wind O^+ peaks are both dominated by magnetospheric ions at both planets and the relative proportions of the Mass-16 atomic ions remain similar, as might be anticipated for escape of atomic ions of similar mass and charge. The Figure 5 comparisons are constructed more for rough qualitative, not precise quantitative, comparisons as the amount of data at Earth is more comprehensive than at Saturn and, for this initial report we use fairly rudimentary fitting procedures. Mass-16 atomic ion ratios (N^+ to O^+ at Earth and C^+ and N^+ to O^+ at Saturn) are nearly identical in the different regimes, suggesting similar escape probabilities and solar wind interactions for the $^{16}M^+$ ions. This does not imply that the magnetospheric escape mechanisms are identical, although they may be, irrespective of the factor of ~10 difference in magnetospheric scales. For Mass-30 ions the detection situation is different, being complicated at Earth by the presence of the lunar Mass-30 PUI. The nearly flat, double-peaked Mass-30 ion SHEATH PHA distribution (blue in 5a) is intermediate between the rounder SPHERE PHA distribution (red in 5a and 5b), with mostly N_2^+ and NO^+, and the distinctly different SW/IM PHA distribution (blue in 5b), dominated by the narrow lunar PUI peak centered near ~28 amu/e. The flat-topped SHEATH feature has significant contributions from lunar Si^+ and Al^+ PUI. We now determine rough estimates of the composition of Earth's Mass-30 ion peaks.

The insets in Figures 5a and 5b demonstrate the superposition of the model distributions used to visually determine fits (orange in insets) approximating Earth's Mass-30 ion composition in the different plasma regimes (separate larger plots with identical axes are in Figure S13 in the SI). Fits are made to the background-subtracted SPHERE (black in inset SP-bk), the SHEATH (blue in inset SH), and the SW/IM (blue in inset SW) Mass-30 ions. SP-bk is the only inset plotted at the same count level as the data, first under the MI peak of the SPHERE data (red curve) near ~32 amu/e and then offset to the left near ~20 amu/e with its component fitting curves; the SH inset is plotted lower than the SHEATH data by a factor of ~40, at the correct M/Q location. Precise quantification of all ion components' contributions in this figure has not been attempted. For fitting shapes, we use (a) Earth's O^+ SHEATH and Saturn's O_2^+ Solar Wind M/Q data peaks as representative atomic and molecular M/Q ion responses, respectively, to model the different regimes' Mass-30 ion shapes, and (b) the SPHERE MI distribution to represent escaped magnetospheric MI in the SHEATH and SW/IM, in which we did not attempt to quantify relative magnetospheric N_2^+, NO^+, and O_2^+ numbers because the relative amounts of lunar Al^+, Si^+, and P^+ is not necessarily well determined as is shown below. Assuming an exponential decrease, the diagonal dashed black line in Figure 5a estimates the SPHERE's O^+ high-M/Q tail underlying the SPHERE's Mass-30 peak. Subtracting this estimate from the SPHERE's Mass-30 peak creates the background-subtracted 'SP-bk' peak, the black histogram underlying the SPHERE Mass-30 peak, and in the SP-bk inset. SP-bk is initially fit with only N_2^+ and NO^+ (both rose-colored) and then with O_2^+ (light-blue colored) fitting shapes, resulting in relative proportions ~43% N_2^+, ~46% NO^+, and ~10% O_2^+. Figures 5a and 5b reveal a distinct transition in Earth's Mass-30 ions from only ionospheric origin MI being apparent in the SPHERE, to mixed escaped magnetospheric MI (still dominant) and lunar atomic PUI in the SHEATH, and then to lunar PUI dominance in the SW/IM. The SHEATH and SW/IM insets use a reduced level escaped-SPHERE MI shape (red) for N_2^+ and NO^+, and different admixtures of Al^+, Si^+, and P^+, the relevant lunar PUI species (purple), in proportions that allow a reasonable overall fit to the Mass-30 data shapes. The relative importance of escaped magnetospheric MI and atomic lunar PUI reverses moving from the SHEATH (with ~64% escaped MI and ~36% PUI) into the SW/IM (with only ~17% escaped MI and ~83% PUI). Our fit to the SW/IM Mass-30 peak demonstrates the necessity of using a relatively enhanced level of O_2^+ to approximate the SW/IM distribution's shape. Given that (1) we cannot uniquely identify peaks for the individual presumed ion species from ~27 to 33 amu/e, that is for Al^+, Si^+, N_2^+, NO^+, and/or P^+, and (2) the counting uncertainty at these count levels is not negligible, we can vary the relative lunar PUI and MI levels in the SW/IM widely. We found that the Mall et al. (1998) lunar PUI distribution fails to approximate the SW/IM data any better than other lunar PUI choices (see Figure S9 in the SI). Nevertheless, one fact, which we will return to below, is clear: A low level of PHA counts, which we can explain using the model O_2^+ peak, is clearly detected in the SW/IM and that cannot be explained by any other currently identified ionospheric or lunar origin ion species. Additionally, as shown in the SW inset in Figure 5b, the model O_2^+ count level relative to N_2^+ and NO^+ is enhanced over its magnetospheric level (see also Figure S13 in the SI). Once the MI are exposed to solar wind flows in the SHEATH and SW/IM, their relative impact dissociation characteristics may become important. However, this study is not designed to answer all questions related to these ions.

Approximately equal ionospheric Si^+ and Fe^+ abundances result from meteoric ablation (Plane, 2012; Vondrak et al., 2008) at Earth. As N_2^+ and NO^+ are commonly observed in ionospheric outflow, Si^+, with a similar mass, should also be observed—possibly more often than the observed Fe^+, attributed to the ionospheric Fe^+ derived from meteoroids. In the background-subtracted SPHERE inset of panel 5a, SP-bk, we show the effect of including a Si^+ component (purple) at the same level as the SPHERE Fe^+. This addition of Si^+ to the SP-bk fit produces a negligible (0.7%) effect on the amount of ${N_2}^+$ needed for a good fit (we note further that the addition of Si^+ degraded our subsequent total SP-bk fitting attempts). Since the O^+ background subtraction results in larger uncertainties at the leading edge of the SP-bk data, ~28 amu/e, the efficacy of adding Si^+ is very difficult to ascertain with the present data set. Si^+ is also a principal observed lunar PUI (Hilchenbach et al., 1992; Mall et al., 1998). As anticipated from lunar sample secondary ion mass spectrum, SIMS, studies (Dukes & Baragiola, 2015; Elphic et al., 1991), lunar PUI Fe^+ is expected to be present near the Moon at slightly lower levels than Si^+. However, while lunar Si^+ PUIs are observed from the Moon to the magnetopause, no Fe^+ was observed in a concerted campaign of near Moon PUI measurements with an instrument functionally identical to ours (Kirsch et al., 1998; Mall et al., 1998).

By normalizing the plasma regime data to their respective peak O^+ counts, we focus attention on species' abundances relative to O^+. One consequence is that the 1-count levels in Earth's SHEATH and SW/IM (blue curves) appear progressively higher compared to the SPHERE (red curves) in panels 5a and 5b, reflecting a progressively significant decrease in O^+ counts with distance from the SPHERE. (Unnormalized versions of the Figure 5 panels are in Figure S13 in the SI.) The same O^+ decrease is apparent for the Sphere (red curve) to Solar Wind (blue curve) comparison at Saturn in panel 5c. That the ratios of N^+ and C^+ to O^+ at Saturn and N^+ to O^+ at Earth remain approximately constant on escape suggests similar magnetospheric escape processes and paths for these heavy atomic ions at both planets, but not necessarily similar specific processes. Secondarily, the Mass-30 ion levels at both planets do not decrease as much as the atomic ion levels suggesting fewer escape losses for the MI, although the presence of lunar PUIs masking escaped MI at Earth complicates a simple, straightforward comparison. Therefore, we address the simpler situation of Saturn's Mass-30 MI first.

Figure 5c compares M/Q histograms of Saturn's Sphere and Solar Wind data. We restricted our survey at Saturn to the Solar Wind regime because magnetopause and bow shock motions appeared to render the Sheath data more difficult to isolate. Saturn's ${O_2}^+$ peaks in the Sphere and Solar Wind show no significant difference in overall shape, whereas the Sphere $^{28}M^+$ peak is not sufficiently higher than the local background count level to accurately determine a possible change in shape, given the limited sample intervals currently available. As noted above, Saturn's C^+ and N^+ ratios to O^+ in the Sphere and Solar Wind are comparable. Conversely, both $^{28}M^+$ and ${O_2}^+$ exhibit relative peak count level increases with respect to O^+. Larger $^{28}M^+$ and ${O_2}^+$ gyroradii with respect to C^+, N^+, and O^+ are consistent with these MI having larger diffusion/transport coefficients than the lower mass ions (e.g., Scholer et al., 2000), resulting in less MI flux decrease relative to O^+. Probable ${CO_2}^+$ in Saturn's Sphere does not appear in the Solar Wind. However, a higher M/Q species evident at ~45–50 amu/e in the Solar Wind does not appear to have a cognate in the Sphere. One might hypothesize that this ion species, close to the mass of Ti^+ (M/Q = 48 amu/e), may be related to Phoebe and its pervasive ring (Verbischer et al., 2009) and does not appear to enter Saturn's magnetosphere in a manner similar to the apparent difficulty of lunar PUI near Earth to pervade Earth's magnetosphere. Note that Fe^+, clearly observed in the Sphere, is absent from the Solar Wind samples we collected for this study. Given the size of Saturn's magnetosphere with respect to Earth's, Fe^+ might be less likely than Mass-30 MIs, for example, expected to escape Saturn's magnetosphere than Earth's, on account of its larger gyroradius, although the opposite seems to be the case, as reported by Mauk et al. (2019), who found that ions with gyroradii much larger than the magnetopause thickness are impeded from fully escaping across the boundary. These preliminary observations suggest that further collection and research of solar wind and magnetosheath ion data near Saturn is needed to determine: (a) extant ion species and (b) whether any Fe^+ escapes from Saturn's magnetosphere. One must remember that the dimensions of Saturn's magnetosphere are approximately an order of magnitude larger than Earth's, that is, 1 Rs ~ 60,300 km, whereas 1 Re = 6,378 km, and $R_{\mathrm{MP,Saturn}}$ ~ 22 Rs, whereas $R_{\mathrm{MP,Earth}}$ ~ 9–10 Re, so The scale of Saturn's system may play a role in these observational results. We now address Saturn's H_2O^+ component, which shows a significant decrease relative to O^+ not seen for any other ion at Saturn or Earth.

We return to the apparent loss of H_2O^+ in the Solar Wind near Saturn. Figure 5c shows that H_2O^+ is depleted with respect to O^+ in the Solar Wind compared to their relative values in the Sphere, whereas $^{28}M^+$ and ${O_2}^+$

are relatively enhanced in the Solar Wind. As this larger relative deficit occurs only for H_2O^+, we interpreted this as likely resulting from stronger solar wind impact dissociation for H_2O^+ than for either $^{28}M^+$ or $O_2{}^+$, resulting from the lower H_2O^+ bond energy. (Please note that OH^+, also present in the W^+ peak, probably dissociates similarly, as its bond energy is lower than that of H_2O^+; see Table S12 in the SI. However, in this work, we have not currently attempted to determine the OH^+ presence at Saturn, be it either inside or outside its magnetosphere.) The Mass-16 atomic ion ratios in Saturn's Solar Wind data are similar those same ratios in Saturn's Sphere data in a manner similar to the situation for N^+ and O^+ at Earth (see Figures 5b and 5c), suggesting that the O^+ peak in the near-Saturn Solar Wind beyond Saturn's bow shock is likely dominated by Saturn's escaped O^+, not interplanetary PUI O^+. Note that all Sphere data from late 2004 to 2007 is shown in Figure 5c (the species ratios for only those Saturn Sphere orbits adjacent to the Solar Wind intervals of Figure 5c are very similar to the overall sum but have poorer statistics; see Figure S11). At and near Saturn, Cassini and CHEMS were fully operational with near-continuous data recording/transmission, whereas during the cruise interval data transmission was at intermittent (see section 2). Because of these different CHEMS operational situations, we have not yet attempted to directly compare these O^+ fluxes to nominal interplanetary data, given the possibly error-prone process of estimating the interplanetary O^+ fluxes during Cassini's cruise to Saturn, which makes a reliable comparison difficult. Clearly, the magnetospheric escape processes at Saturn may be complicated and a more detailed analysis should be pursued in the future when additional Cassini bow shock and magnetopause crossing identifications near Saturn have been determined and verified. Nevertheless, the initial bow shock and magnetopause crossing identifications at Saturn have been critical in enabling this analysis and our considerations and interpretation of the Mass-30 ions' identity outside the planets' magnetospheres. The data have demonstrated that (a) the peak of $O_2{}^+$ M/Q PHA distributions is clearly not centered at the MI's atomic mass, but displaced to M/Q >32 amu/e both inside and outside Saturn's magnetosphere, and (b) the overall shape of the MI PHA Mass distributions is rather similar inside and outside Saturn's magnetosphere, very different observational environments.

Figure 5d shows the clear TOF differences between Mass-30 ions in Earth's SPHERE and SW/IM regimes (collected over ~6 and ~21 years, respectively) at three widely spaced electrostatic deflection step voltages. The TOFs of SPHERE MI data (red), mostly $N_2{}^+$ and NO^+, are generally longer than the TOFs of SW/IM data (blue), where there is a significant contribution from atomic Si^+ lunar PUIs. As explained above in section 2, MIs travel slower than the atomic ions on account of losing additional energy in the carbon foil. These data demonstrate the significant differences between atomic and molecular ion responses and will be useful in separating the lunar and terrestrial origin ions in subsequent, dedicated studies.

3.3. Geomagnetic and Solar Activity Dependence at Earth

Figure 6 shows the overall geomagnetic and solar activity dependence of long-term average 3-hr PHA count sums of the MI channels, N^+, O^+, and Fe^+. These 3-hr PHA count averages are rough guides to different species' occurrence rates, likely more accurate at low levels and underestimates of actual species rates at their highest levels. However, they provide guidance as to species' flux dependence on geomagnetic and solar activity. Data collected over all regimes are plotted versus Kp in Figure 6a and F10.7 in Figure 6c with $^{28}Mq^+$ and $^{30}Mq^+$ ions separated. Kp averages are taken over the −, o, + range of integer Kp values, where, for example, Kp = 3 in the plot includes Kp = 3−, 3o, and 3+. Parallel heavy dashed lines in Figures 6a and 6c are drawn parallel to the approximate N^+ and O^+ slopes at high Kp and at $F10.7 > 100 \cdot 10^{22}$ W/m²/Hz, respectively. These lines represent the nominal moderate-to-high activity ionospheric outflow rate increase of dominant heavy ionospheric atomic ions with respect to Kp and F10.7, that is, the terminal outflow rate. They are meant to guide the eye and to highlight similarities and differences of ion group geomagnetic and solar activity dependences. Correlations of the ion groups with Kp are positive overall. At low Kp, Fe^+ increases with Kp less rapidly than any of the other species' average rates, all of which are similar. The O^+ and N^+ outflow Kp rates relax to that of Fe^+ at high Kp. The overall Fe^+ Kp rate increase changes the least of all species, being roughly characterized overall by the terminal outflow rate. The Mass-30 and Mass-40 ions' Kp rates of increase never relax to the average terminal outflow rate of O^+, N^+, and Fe^+; instead, they increase significantly in the highest Kp range. The overall Mass-40 ion Kp rate increase accelerates more rapidly than any other species at low Kp, relaxes somewhat at mid-Kp, and then accelerates to be the fastest outflow Kp rate at $Kp \geq 5$. Data collected separately in the SPHERE and SW/IM

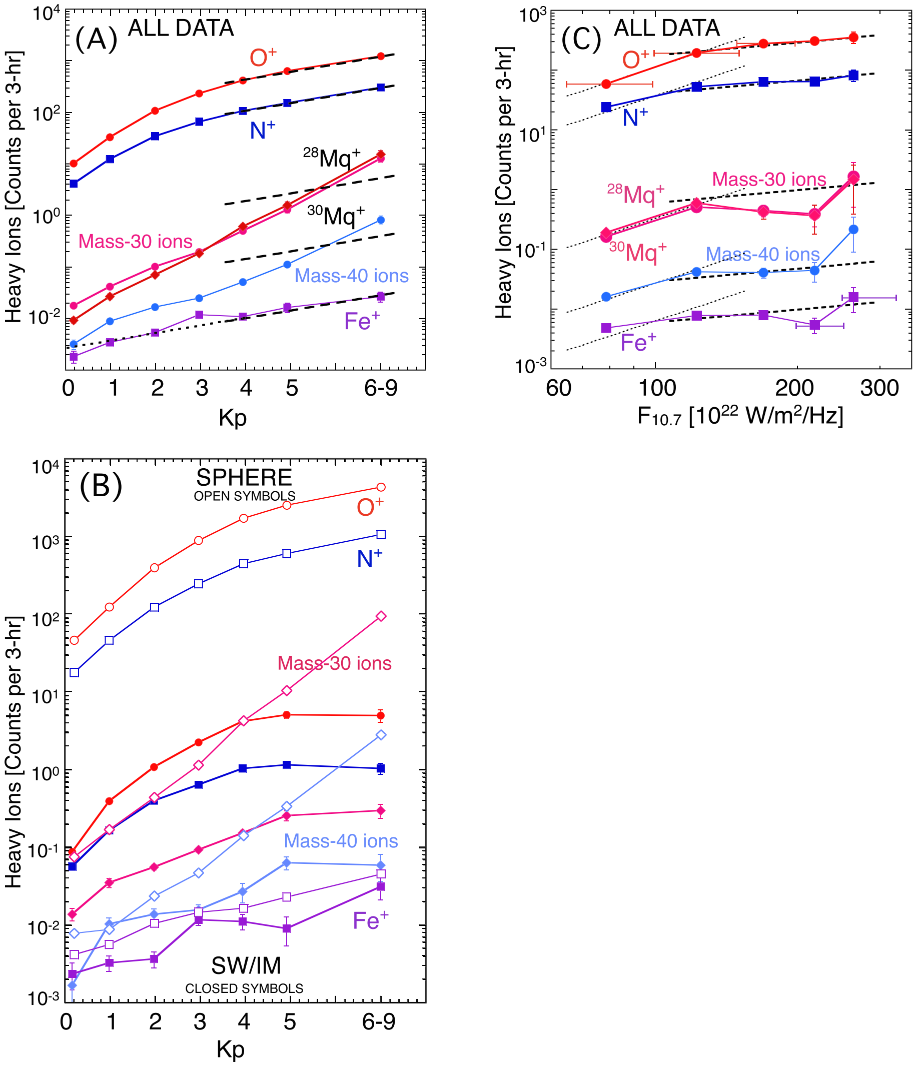

Figure 6. Averages of suprathermal (~87–212 keV/e) N^+, O^+, Fe^+, Mass-30 ions ($^{28}Mq^+$ and $^{30}Mq^+$) and Mass-40 ions 3-hr PHA count sums are plotted versus interval averages of (A, B) Kp and (C) $F_{10.7}$ values from 1995 to 2015. In (A) and (B), all data are shown. In (B) the data are from two plasma regimes, SPHERE (open symbols) and SW/IM (closed symbols). Uncertainties, standard error of the mean, are generally smaller than the point size. Horizontal bars in (C) indicate $F_{10.7}$ ranges. Kp averages are over the -, o, + range of the Kp index integer values. Dashed and dotted lines in (A and C) are intended to guide the eye in comparing the heavier ions to N^+ and O^+ (see text). The dotted extension of the Fe^+ line in (A) highlights the outlying Kp = 3 average which is also apparent in the SW/IM data.

regimes are plotted as open (closed) symbols versus Kp in Figure 6b, where we note that both Mass-40 ions and Fe^+ may be insufficiently sampled in the SW/IM. SPHERE and SW/IM intervals dominate the magnetospheric ion data set because it is there, in the magnetosphere and the solar wind, respectively, where fluxes are the highest in the first case and where the satellite spends the most time in the second, respectively. In Figure 6b, (a) monotonic Kp rate increases are evident for all species in the SPHERE at all Kp values, where the Mass-30 and Mass-40 ion increases are the strongest and Fe^+ is the weakest; (b) all SW/IM Kp rate profiles except that of Fe^+ are generally similar, relaxing, even decreasing slightly in two cases, at high Kp; (c) Fe^+ experiences a large increase at Kp = 3 in the SW/IM but then decreases until Kp = 5, above which it resumes increasing. The continual strong rate of increased Mass-30 and Mass-40 ion flux in the SPHERE is uniquely different from that of O^+, N^+, and Fe^+ and is consistent with the findings of Lennartsson et al. (2000) and should be studied in the future.

Figure 6c shows that while O^+ and N^+ F10.7 dependences are similar, only O^+ increases monotonically with $F_{10.7}$ unambiguously. N^+ is more similar to O^+ than to the heavier ions, although its mid-$F_{10.7}$ points barely increase. In contrast, the Fe^+ dependence on F10.7 is more similar to that of Mass-30 and Mass-40 ions than to N^+ or O^+, even though the Fe^+ and N^+ dependence from low to mid F10.7 values is very similar. From ($80 \leq F_{10.7} \leq 120$) 10^{22} W/m^2/Hz, all species $F_{10.7}$ rates appear to increase, although each with individual characteristics. O^+ and Mass-30 ions increase more strongly at low $F_{10.7}$, N^+, and Fe^+ more weakly. Mass-30 and Mass-40 ion $F_{10.7}$ rates decrease noticeably at (120 to 170) 10^{22} W/m^2/Hz. At ~(120 to 220) 10^{22} W/m^2/Hz, mid-$F_{10.7}$ values, Mass-30, Mass-40, and Fe^+ ion $F_{10.7}$ rates all decline and then increase significantly at the highest $F_{10.7}$ value. The following discussion of lunar ion fluxes should increase our understanding of the differences. Below, we briefly introduce, define, and characterize relevant information we have found in our data regarding the lunar PUI background in the Mass-30 ion data before characterizing MI variations identifiable in the Mass-30 and Mass-40 ion channels near Earth.

4. Lunar PUI Fluxes Near Earth

4.1. Lunar PUI Separation/Identification

In section 3 we demonstrated that the Mass-30 $^{28}Mq^+$ and $^{30}Mq^+$ ion channels both contain significant atomic lunar PUI components. The map of Geotail orbit plasma regimes in Figure 7a shows the Earth (blue dot at center), the average locations of the SPHERE, SHEATH, and SW/IM plasma regimes (as described in section 2.0.1), the Moon's orbital variation range, and a number of Geotail $R <$ ~30 Re orbit segments for an overview perspective. Two spatial features/conditions are important for considering possible lunar influence: (1) The Moon's Lunar orbital Local Time (or LLT) “Sector 3” range, $10 \leq$ LLT ≤ 14 hr (1/6 of the Moon's full orbit), which includes lunar orbit locations where the Moon is more or less “directly” sunward of the Earth and the Geotail orbits to which it can most readily contribute PUIs via convection; and (2) the heavy ion Lunar Wake, drawn here with a broad, ~25 Re, width to include heavy ions with masses up to SiO^+, $CO_2{}^+$, or Fe^+, for example, suprathermal energy heavy ions with large gyroradii in the nominal (~7–9 nT) interplanetary magnetic field at ~1 AU. In the map near Earth, dotted traces and large black and white squares indicate 37 Geotail orbit segments that are ≥24 hr long and end at the Fe^+ measurement (squares). The orbit segments include 42 Fe^+ PHA measurements in the SPHERE (33 black) and in the SHEATH (9 white) obtained during low to moderate geomagnetic and solar activity conditions. A PHA color spectrogram for the data from these orbits is shown in Figure S5 in the SI. The orbit intervals were selected by Christon et al. (2017) for their characteristic of having a low presence of PHA counts in the M/Q range of Mass-30 ions (which may include Al^+, Si^+, $N_2{}^+$, NO^+, $O_2{}^+$, P^+, and Fe^{+2}), specifically to exclude possible Fe^{+2} charge-exchanged from high-charge-state solar wind iron, $Fe^{+7:+14}$, prior to the measurement of a Fe^+ in the SPHERE or SHEATH. Use of this observation interval selection scheme near Earth under low Mass-30 ion (e.g., Si^+) conditions is germane to arguments regarding lunar PUIs because various laboratory studies have suggested that Fe^+ is an expected product of lunar soil irradiation by typical solar wind energy ions through secondary ion mass spectrometry (e.g., Dukes & Baragiola, 2015; Elphic et al., 1991). Lunar PUI Fe^+ has been anticipated in lunar ion observations and modeling (e.g., Poppe et al., 2016; Sarantos et al., 2012; Yokota & Saito, 2005), but lunar PUI Fe^+ has not yet been observed near the Moon with instruments that are designed to measure Fe^+ (e.g., Kirsch et al., 1998; Mall et al., 1998; Poppe et al., 2016; Sarantos et al., 2012; Yokota & Saito, 2005). Geotail/STICS has measured Fe^+ near Earth. The selected orbit segments include times when the Mass-30 ion counts near Fe^{+2} (M/Q ~28 amu/e, M ~ 50–70 amu) were consistent with the surrounding, extant, low background-count levels representative of relatively low-to-moderate geomagnetic and solar activity intervals near-Earth (Christon et al., 2017). The nine large white squares here, seven in the SPHERE and two in the SHEATH, are ~21% of the 42-count Fe^+-sample and represent Fe^+ observations made at times when the Moon was sunward of Earth in the ~10–13 hr LLT range (LLT Sector 3). The large black squares represent Fe^+ observations from the other select orbit segments when the Moon was not sunward of Earth and it was in locations around the Earth from which one would not necessarily expect to observe lunar PUI transported via convective processes to the SPHERE. (The red dots show the other Fe^+ measurement locations.) The nine Fe^+ counts measured when the Moon was in LLT Sector 3, as a portion of the 42 total PHA events, are not significantly different from the overall average seven total Fe^+ counts per LLT Sector, consistent with there being no elevated lunar PUI signal in LLT Sector 3. This argues that

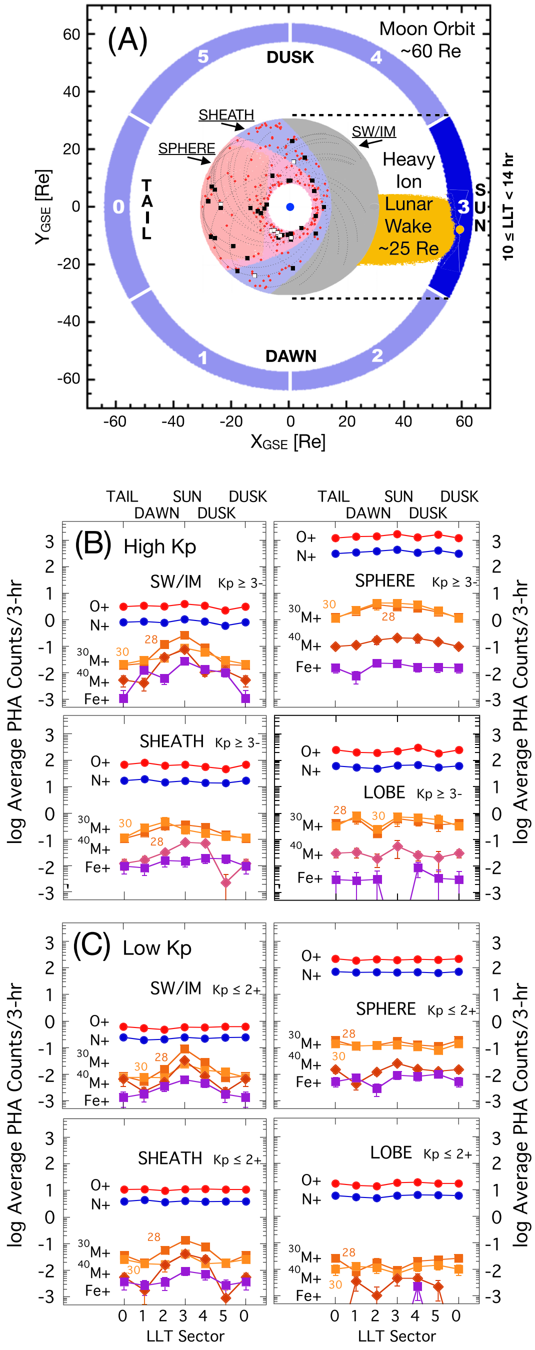

Figure 7. (A) A sketch of the Earth (blue dot at center), the Moon's orbital range, and Geotail orbital range, ~9 < R < 35 Re. Two spatial criteria for considering possible lunar pickup ion influence in Geotail/STICS suprathermal (~87–212 keV/e) ion measurements are the lunar local time (LLT) and the 'Lunar Wake'. LLT marks the orbital location of the Moon with respect to the Earth-Sun line. At 10 ≤ LLT ≤ 13 hours, LLT-Sector 3, the Moon is sunward of Geotail's nominal orbital X_{GSE} -Y_{GSE} range. From favorable orbit locations ~60 Re sunward of Earth, the Moon can convectively contribute pickup ions to our SW/IM data near Earth. The 'Lunar Wake', drawn here with a ~25 Re width to include heavy ion (e.g., CO_2^+ or Fe^+) gyroradii in the nominal (~7-9 nT) interplanetary magnetic field at 1 AU, is probably always present, varying in strength, and is likely important in supplying lunar PUI to near-Earth locations. Selected segments of Geotail orbits, the dotted traces near Earth, terminate when an Fe^+ was observed during low to moderate solar/geomagnetic conditions. White (black) squares indicate Fe^+ observations obtained when the Moon was (not) in LLT-Sector 3. Red dots show other measured Fe^+ data. Arrows point from underlined labels to three near-Earth plasma regimes. The LOBE (not shown) overlies the SPHERE. (B,C) Four panels at (B) High-Kp and (C) Low-Kp levels enable investigation of some possible observable effects of lunar PUIs intermixed with Earth's escaped ionospheric ions which are related to the Moon's orbital location. The effects differ between observations made in the four near-Earth plasma regimes used in this study.

the Fe^+ observed in and near the SPHERE at low to moderate geomagnetic activity levels is unlikely to be of lunar origin at times when few Mass-30 ions of either ionospheric or lunar origin are measured in the SPHERE. Further, PHA data from these orbit segments (shown in Figure S5 in the SI, and below) argue that the Fe^+, combined with the Mass-30 ions' M/Q distribution from these orbits, is more consistent with an ionospheric, rather than lunar origin. This does not imply that lunar PUI Fe^+ may not be produced during intervals of more intense geomagnetic and/or solar activity. As we comment below, lunar PUIs may be present in the SPHERE during disturbed conditions, but currently, we have not yet characterized their proportion or occurrence likelihood.

4.2. Ion Flux Variations Related to Moon Location

Figures 7b and 7c show average N^+, O^+, Fe^+, Mass-30 ($^{30}M^+$), and Mass-40 ($^{40}M^+$) ion data collected during high-Kp ($Kp \geq 3-$) and low-Kp ($Kp \geq 2+$) intervals, respectively, in each of the plasma regimes for times when the Moon was in each LLT Sector, irrespective of solar activity level. The highest Kp intervals ($Kp \geq 8o$) were excluded from these initial averages because of spatial sampling effects. In the following, for a specific ion channel, we consider a “signal” to be a LLT Sector PHA count average higher than the channel's overall average having a statistically significant difference from the other averages in that species' Kp and plasma regime selection grouping, such as the $^{30}M^+$ and $^{40}M^+$ ions in the high-Kp and low-Kp SW/IM panels. The analysis is designed so that a significant lunar PUI signal should result in an LLT distribution that peaks at LLT Sector 3, especially in the SW/IM and SHEATH data. A similar result should be evident for the heavier ions as a result of the solar wind convection anisotropy, although a convective signature would likely dissipate in SW/IM and the SHEATH Sectors farther from Sector 3 and disappear while the spacecraft was in the SPHERE and the LOBE. One would anticipate a strong PUI signal for $^{40}M^+$ ions, which we presume are dominated by lunar PUI in SW/IM and SHEATH data, but obscured in the SPHERE by backgrounds (see Figure 5 and Figure S3 in the SI). A lunar PUI signal should add to the convective anisotropy peak in all LLT Sectors, but primarily in the sunward LLT Sector 3. We take Figure 5's N^+ and O^+ distributions in the SW/IM and SHEATH to represent the “lighter-ion” escaped, or escaping, magnetospheric ion signal; $^{40}M^+$ in the SW/IM and SHEATH to represent a lunar PUI signal; and Fe+ in the SHEATH to represent a convective signal. Please note that distinct, single-LLT-Sector variations, such as a discontinuous large increase or decrease in a single LLT Sector, may result from either (a) unintended inclusion or exclusion of solar related particle events (flares, shocks, and/or CMEs) inadvertently missed in the data inspection/inclusion procedures or (b) low counting statistics. Several overall aspects shown in the panels are (a) $^{16}M^+$ species do not exhibit any outstanding LLT-Sector peaks in any regime and no statistically significant differences throughout, although the LLT-Sector 3 average is just significantly different with respect to the LLT-Sector 2 average at low Kp and nearly so at high Kp; (b) $^{30}M^+$ and $^{40}M^+$ ions have highly statistically significant peaks centered on LLT-Sector 3 in the SW/IM and SHEATH, which are more pronounced than any signal possibly present for $^{16}M^+$ ions and Fe^+; (c) SW/IM $^{30}M^+$ and $^{40}M^+$ ions likely have strong lunar PUI contributions, as evidenced by their strong, broad peaks centered on LLT-Sector 3 in the SW/IM at high Kp and for $^{40}M^+$ ions in the SHEATH, although see (d); (d) at high Kp MI^+ likely dominate SHEATH $^{30}M^+$ ions as suggested by the somewhat uniform overall distribution (more comparable to the $^{16}M^+$ ion data than at low Kp), whereas lunar PUI likely dominate SHEATH $^{30}M^+$ ions at low Kp as indicated by the prominent LLT-Sector 3 peak; (e) the $^{40}M^+$ ions in the SPHERE appear to be dominated by random background counts; hence, the uniform distribution; (f) Fe^+, for which LLT-Sector 3 is sometimes stronger and LLT-Sector 0 is sometimes weaker in the various plasma regimes, seems generally consistent with convective anisotropies, not a lunar PUI source; (g) for high-Kp averages, Fe^+ may have a lunar PUI component in SW/IM data on account of the statistical significance of LLT-Sector 3, which is higher than the next three highest Fe^+ high-Kp averages, the difference is significant for only LLT-Sector 5; (h) Fe^+ appears to have a strong convective anisotropy in the low-Kp SW/IM averages; and (i) in the LOBE, no species shows a large overall variation and very little Fe^+ is observed. Additionally, comparison of the SW/IM Fe^+ LLT-Sector 3 average to the other Fe^+ LLT-Sector averages in the various regimes (see Table S6 in the SI) suggests that despite similar enhanced levels at and near LLT-Sector 3, the Fe^+ count differences are much less extreme than those of $^{30}M^+$ and/or $^{40}M^+$ ions, tending possibly toward the uniformity characteristics of $^{16}M^+$ ions than lunar PUI. This brief assessment of the ion channels suggests for SW/IM: A clear lunar PUI/convective signal in $^{30}M^{+}$ and $^{40}M^{+}$; possible convective signals in $^{16}M^{+}$; a broad convective and possible lunar PUI signal in Fe^{+} at high Kp; SHEATH: clear $^{40}M^{+}$ and probable/possible $^{40}M^{+}$ and Fe^{+} convective and/or lunar PUI signal; SPHERE: broad, higher $^{30}M^{+}$ sunward LLT-Sector levels at high Kp suggest lunar PUI leakage into the SPHERE; background dominated $^{40}M^{+}$ shows a possible lunar PUI signal; SPHERE Fe^{+} is nominally as uniform as SPHERE $^{16}M^{+}$, with no statistically significant inter-average differences; and LOBE: statistically significant $^{30}M^{+}$ and $^{40}M^{+}$ and possible Fe^{+} PUI signals in LLT-Sector 5.

4.3. Mixing of MI and PUI Near Earth

Separation of the superposed $^{28}Ma^{+}$ ions' ionospheric N_2^{+} and lunar PUIs dominated by Si^{+}, in the near-Earth SW/IM's Mass-30 PHA distributions, is demonstrated in Figure 8 using two different methods. The solid curves in Figure 8a are smoothed fits to the near Earth SW/IM plasma regime ion data from Figure 4d. O^{+} and N^{+} are again shown for comparison. As noted above in the discussion of Figure 4, Earth's $^{28}Ma^{+}$ and $^{30}Ma^{+}$ SW/IM data are more complex than, and not similar to, the comparable $^{28}Ma^{+}$ and $^{30}Ma^{+}$ SPHERE data as a result of the presence of lunar PUIs. For example, in addition to ionospheric N_2^{+} and NO^{+}, the $^{28}Ma^{+}$ and $^{30}Ma^{+}$ channels will also contain some lunar Si^{+}, Al^{+}, and P^{+}. As a first step, we first scale the $^{30}Ma^{+}$ distribution shape upward by a factor of 1.55 (the purple dashed curve) in order to extract the most important differences between the $^{30}Ma^{+}$ and $^{28}Ma^{+}$ distributions. At this upward scaled level, the differences between the lower portions of the scaled $^{30}Ma^{+}$ curve and the $^{28}Ma^{+}$ curve (those segments below the gray horizontal area) are statistically negligible, but now comparable. Subtracting the scaled $^{30}Ma^{+}$ curve (purple dashed curve) from the $^{28}Ma^{+}$ data (orange solid curve) leads to an initial crude estimate of $^{28}Ma^{+}$ lunar PUIs, the black dashed curve labeled "Estimate of lunar PUI" in panel 8a. The shape of the Estimate's peak is very similar to that of the O^{+} peak, as shown by the shifted O^{+} peak (red dashed curve) centered at the Estimate's peak. But for a distinct shoulder at ~15–24 amu, the curves' similarities argue that the SW/IM $^{28}Ma^{+}$ ions are likely dominated by a single atomic ion with a shape similar to that of O^{+}. This result is encouraging, because Si^{+} dominates the lunar Mass-30 PUIs measured by Hilchenbach et al. (1992) and Mall et al. (1998), measurements we will address in the next section.

A more detailed investigation of the $^{28}Ma^{+}$ peak is demonstrated in Figures 8b, 8c, and 8d, in which model atomic ion PHA distributions are used to fit the observed $^{28}Ma^{+}$ data (orange solid curve). First, we determined that the atomic ion Mass distributions of SW/IM O^{+} and solar wind $Fe^{+5:+11}$ Mass distributions are similar, but not identical (see Figure S7 in the SI); that is, the $Fe^{+5:+11}$ ions' shape is slightly narrower. However, given that the shape of the lunar PUI component in Figure 8a was very similar to that of O^{+} and there is presently no straightforward method to determine the shape of an individual Mass-30 ion's Mass distribution, we simply use the O^{+} shape as our model atomic ion shape in the following analysis. We first use this model shape to visually determine the contributions from lunar PUI Al^{+}, Si^{+}, and P^{+} at levels consistent with the proportions of relevant lunar PUIs from Mall et al. (1998) combined with a scaled representation of an admixture of MI-dominated $^{28}Ma^{+}$ and $^{30}Ma^{+}$ SPHERE data assuming escaped magnetospheric MI populations do not change significantly during the escape process (consistent with the distributions of escaped Saturn MI in Figure 4). The heavy dot-dash curves labeled "Fit" in Figures 8b, 8c, and 8d approximate, as best we can, the expected shape of our $^{28}Ma^{+}$ SW/IM data. (Please note that we use the capitalized word Fit in this paragraph to refer to these "Fit" curves displayed in Figure 8.) The mixture of Mass-30 atomic ion species in lunar PUI from Mall et al. (1998) data shown in Figure 8b is $Al^{+} : Si^{+} : P^{+} = 0.72 \pm 0.09 : 1.00 \pm 0.12 : 0.51 \pm 0.07$ (106: 148: 76 PHA counts). These ratios are derived from our assessment of their Figure 1 PHA histograms (shown below and in Figure S10). After subtracting this mixture of ionospheric MI and lunar PUI, the residual (the heavy solid black curve in Figure 8b, lower panel) demonstrates that we can account for most of the observed SW/IM $^{28}Ma^{+}$ shape within one standard deviation of the Data curve (1, 2, and 3 standard deviations shown as dashed curves in the bottom panels of Figures 8b, 8c, and 8d). However, two ranges of wider Fit-Data mismatch remain: One at ~15–24 amu and the other at ~38–100 amu. Presuming that the lunar PUI composition might change over different phases of a solar activity cycle and the Mall et al. data were obtained near the minimum solar activity of 1994–1998, we then sought a different, more optimal combination of lunar PUIs required to fit our Data (obtained over two full solar cycles), which is shown the PUIs incorporated into the Fit in Figure 8c. The PUI ratios for this optimal PUI Fit are $Al^{+} : Si^{+} : P^{+} = 0.89 : 1.00 : 0.63$. The Data-Fit mismatch below ~40 amu is slightly better, but

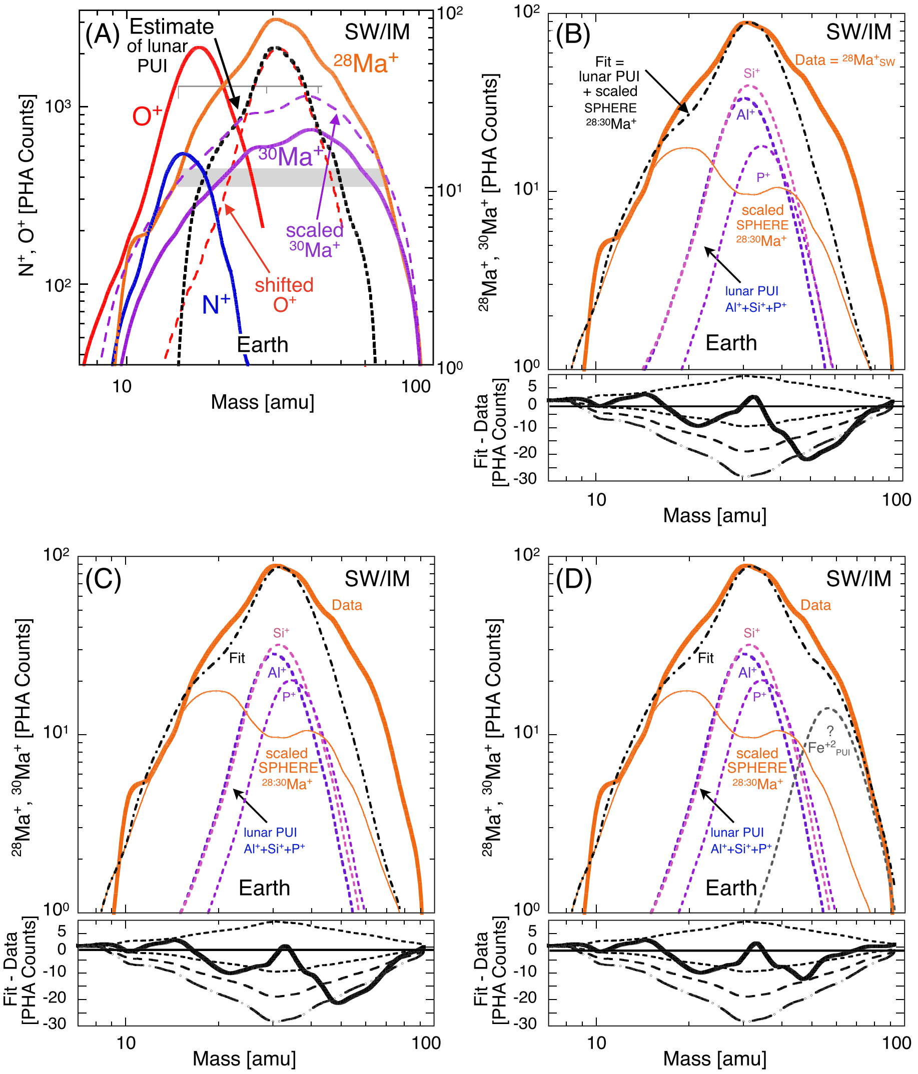

Figure 8. The superposition of the PHA distributions of lunar pickup ions, PUI, mostly Si$^+$, and ionospheric N_2^+ in the near-Earth solar wind, SW/IM, PHA distributions is investigated using two different comparisons. (A) The suprathermal (~87–212 keV/e) ion data are all from the SW/IM plasma regime near Earth. Solid curves are smoothed, interpolated fits to the data in Figure 3D. The shape of neither the ^{28}Ma$^+$, 28-amu (orange), nor ^{30}Ma$^+$, 30-amu (purple), ion mass distribution, is similar to the corresponding bimodal SPHERE MI shapes at Earth or Saturn (see the scaled SPHERE shape in panel 8B and Figure 4C). Expecting a smaller lunar PUI background in the ^{30}Ma$^+$ data based on previous measurements by Mall et al. (1998), we approximate Earth's MI portion of the ^{28}Ma$^+$ SW/IM data by scaling the ^{30}Ma$^+$ curve upward (dashed purple curve), and subtract this from the SW/IM ^{28}Ma$^+$ (orange) curve. This results in the black dashed curve, a crude estimate of lunar PUI (mostly Si$^+$ and Al$^+$) contributing to the ^{28}Ma$^+$ data, which has a shape similar to the SW/IM O$^+$ (shown also as the red dashed curve shifted to ~30 amu). Differences between the Fit and Data below the gray horizontal area drawn at ~10-12 counts are not statistically significant. (B, C, and D) In a different treatment investigating possible components of the SW/IM ^{28}Ma$^+_{SW}$ data, we construct a Fit from a scaled combination of Earth's SPHERE MI, ^{28}Ma$^+_{SP}$ and ^{30}Ma$^+_{SP}$, ions added to different ratios of relevant lunar atomic PUI populations. Al$^+$, Si$^+$, and P$^+$ were identified by Mall et al. (1998) as the principal Mass-30 ions. Separately, in a panel below each set of PUI and Fit curves, the difference between our Fit and the measured ^{28}Ma$^+_{SW}$ ions is shown along with dashed +1 to -3 standard deviation curves for the Data. In panel 8B, we use our derived Mall et al. relative proportions (see text) and in panel 8C, we adjust the PUI Al$^+$, Si$^+$, and P$^+$ relative proportions to get a better visual fit. Finally, in panel 8D, in order to further reduce the Fit---Data differences, we combine those best-fit lunar PUI proportions with a hypothetical lunar Fe^{+2} population to compare to the Data.

the significant Data-Fit mismatch peaking at M ≈ 50 amu remains and does not appear to be explained by our current estimate of ion composition candidates. Any solution to the mismatch must have the M/Q of ~28 amu/e and a Mass between ~50 and ~60 amu. The only reasonable physical explanation we arrived at is that we may be measuring a population of doubly charged iron, Fe^{+2}, which has M = 56 amu and M/Q = 28 amu/e. Fe^{+2} has been identified at lower energies in coronal mass ejection solar wind flows (Gilbert et al., 2012) and as a possible interstellar PUI generated by and transported with the solar wind (Taut et al., 2015). Recent analysis also revealed that Fe^{+2} is a component of nanodust particles in space-weathered lunar soils (Thompson et al., 2016). Therefore, we added a Fe^{+2} model PUI component to our admixture and found that the overall agreement with data improved as shown in Figure 8d. The relative Mass-30 PUI ratios with this addition to our optimal PUI Fit is $Al^+ : Si^+ : P^+ : Fe^{+2} = 0.89: 1.00: 0.63: 0.44$. Next, we briefly examine Mass-30 ion upstream measurements; that is, sunward of the foreshock region of the SW/IM data, a regime where bow-shock-related effects might be less evident.

4.4. Earth's Foreshock Region

Figure 9a demonstrates that even in the presence of lunar PUI in the same mass range, small amounts of the three ionospheric molecular ions, N_2^+, NO^+, and O_2^+ are likely visible at $X_{GSE} \geq 20$ Re out to $R \sim 30$ Re, the farthest sunward locations sampled by Geotail. These ion data are obtained at ≥5 Re sunward of the nominal bow shock subsolar distance—locations nominally sunward of direct bow shock the bow shock interactions with the solar wind or lunar PUI, even though some backscattered ions and upstream wave and field effects are probably present (Kis et al., 2004; Mitchell et al., 1983). Additionally, it is well documented that at times, bursts of keV-energy, low-charge-state ions (including N^+, O^+, and O^{+2}) can be observed at ~35–1,750 Re sunward of Earth (e.g., Christon et al., 2000; Kronberg et al., 2011; Posner et al., 2002). These burst intervals add to, but do not dominate, long-term average flux information sunward of the bow shock, which is specifically of interest here. Some of the doubly charged O^{+2} though may first reside in Earth's O^{+2}-rich plasmasphere (e.g., Farrugia et al., 1989) before transport to dayside magnetosheath reconnection sites via plasmaspheric plumes (e.g., Borovsky & Denton, 2006). These burst intervals add to, but do not necessarily dominate, the long-term average fluxes sunward of the bow shock of interest herein. Over 40% of all SW/IM Mass-30 observations are obtained sunward of $X_{GSM} = 20$ Re where Geotail dwells longest at its ~30 Re apogee, so this selection at ~5–15 Re upstream of the average bow shock location can reveal significant information about the solar wind as minimally affected by upstream bow shock related effects that our data set can provide. Figure 9b shows the lunar PUI data from Hilchenbach et al. (1992) and Mall et al. (1998), the shaded and line histograms, respectively, for direct comparison of lunar PUIs slightly closer to Earth and near the Moon, respectively. Hilchenbach et al. (1992) selected antisunward flows at ~18 Re, ~3 Re sunward of the average bow shock location, during several intervals when the moon was approximately sunward of their spacecraft. Their data are the most comparable to ours, both data sets having been accumulated in approximately the same location, although for different purposes, with different methodologies, and under different solar activity conditions. They noted the presence of O^+ and suggested the presence of Al^+, Si^+, or S^+ (focusing on their counts near 32 amu/e while rejecting detection of Earth's MI) as possible candidate ions for the observed Mass-30 ions, as well as a few ions with marginal statistics measured from 40 to 54 amu/e that they suggested were consistent with Ar^+, Ca^+, or Fe^+. Mall et al. (1998) presented two PHA histograms of lunar PUI data in their Figure 1. A lunar-radial variation was found, where lunar PUI counts decreased with increasing distance from the Moon. On account of the low number of counts in their histograms, we summed their two M/Q histograms, which widened their O^+ to Si^+ energy range to ~20–200 keV/e. We focus on their Mass-30 species, suppressing any discussion of other species they discussed with respect to their data (Mall et al. did not mention Fe^+). Their Moon-related measurements were obtained sunward of Earth at ~17–150 lunar radii from the Moon, which is at ~60 Re from the Earth. The mixture of Mass-30 PUI atomic ion species in our summing of their data normalized to Si^+ (in absolute counts) is $Al^+ : Si^+ : P^+ = 0.72 \pm 0.09: 1.00 \pm 0.12: 0.51 \pm 0.07$ (106: 148: 76 PHA counts, see also Figure S10 in the SI). In order to center the three data sets' O^+ peaks, we translated the M/Q locations of both the Hilchenbach et al. and Mall et al. data to slightly lower M/Q values by ~0.5–1 amu/e. All three data sets are limited by low counting statistics, different observation locations, and widely different solar activity conditions. That is, the Hilchenbach et al. (1992) and Mall et al. (1998) data were both obtained during solar activity minimum conditions, whereas our data encompass all data obtained over two solar cycles, and as seen in Figure 6, lunar ion production is likely enhanced during the disturbed solar conditions, conditions which also result in enhanced ionospheric outflow.

Finally, Figure 9c shows that sunward of the bow shock O^+ and N^+ still dominate the omnidirectional heavy ions and the Mass-30 ion peak extends from ~25 to ~35 amu/e. We note that O_2^+ is likely evident

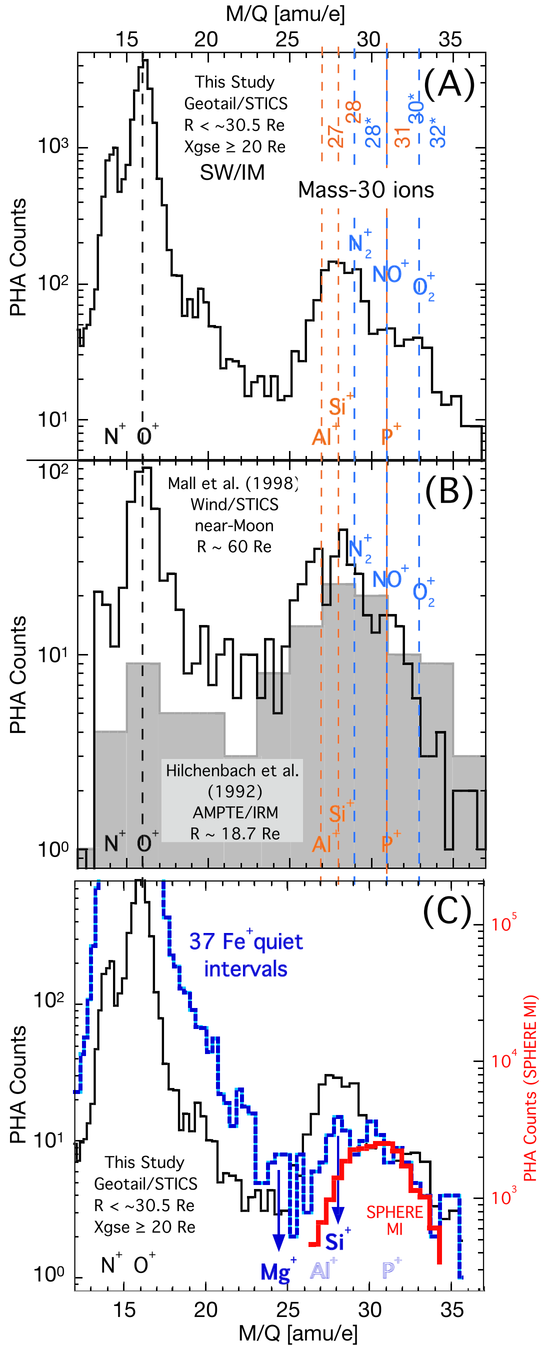

Figure 9. Histograms of N^+, O^+, and Mass 30 ion PHAs ordered by M/Q from (A) this study's farthest upstream Geotail/STICS data compared to that from (B) Mall et al. (1998) and Hilchenbach et al. (1992). Mass-30 molecular ion, MI (blue text), and lunar pickup ions, PUI (tan text), masses are identified. The MI generate higher M/Q values (asterisked values) than atomic ions of the same mass (see text). Our farthest upstream ~87-212 keV/e ion data were measured sunward of the bow shock at $X_{GSE} \geq 20$ Re out to R ~ 30.5 Re over approximately 2 full solar cycles. Hilchenbach et al. (1992) measured ~80-226 keV/e lunar PUIs sunward of the bow shock at $R \leq 18.7$ Re over 3 months in late-1985. Mall et al. (1998) presented two PHA histograms of Wind/STICS measurements of ~20-200 keV/e lunar (PUI) obtained from 1995 to 1997 sunward of Earth near the Moon at >17 lunar radii. Given their study's lower number of counts, we summed their two PHA histograms into one (see text). N^+ and O^+ are shown for reference. Both the Hilchenbach et al. (1992) and Mall et al. (1998) data were obtained during minimum solar activity conditions. (C) This panel compares our farthest upstream data (black) to that from the overall SPHERE shape (red), which is dominated by MI, and to the 37 low to moderate solar/geomagnetic condition orbits used for the traces in Figure 7A (blue). Si^+ is both a major ionospheric origin ion from IDPs (Plane et al., 2016) and one of the major lunar pickup ions (e.g., Mall et al., 1998; Poppe et al., 2016). The quiet interval data show little similarity to our farthest upstream data, but do show evidence of peaks at Mg^+ and Si^+ (ionospheric ions) superposed on ions with the overall shape of the SPHERE data, but Al^+ and P^+ (lunar pickup ions) are not evident. The data are translated vertically to match values near ~32 amu/e.

by the contiguous elevated count levels up to ~34–35 amu/e in the two near-Earth data sets measured sunward of the bow shock, ours and Hilchenbach et al. (1992). Therefore, these selected SW/IM data obtained somewhat upstream of the bow shock contain straightforward evidence of some O_2^+ in addition to $P^+||NO^+$. Our study and Hilchenbach et al. (1992) both measured these data with similar time-of-flight versus total energy instruments, and it appears that both instruments reveal similar evidence sunward of the bow shock of an ion at ~2–3 amu/e higher than the likely P^+ location—an ion that we suggest is O_2^+ given our current understanding of these instruments' response to MI. That is, the near-bow shock data are not consistent with being explained alone by lunar PUI P^+, which should only mask a portion of the NO^+. While there is no obvious evidence of O_2^+ in the Mall et al. near-Moon data, there is evidence of O_2^+ in our data. Because of the small O_2^+ abundance relative to N_2^+ and NO^+ in the SPHERE, O_2^+ is difficult to detect there, being masked by NO^+ and/or various magnetospheric background signals present in this initial survey in which we have presented data from all geomagnetic and solar activity levels (see, for example, the color spectrograms in Figure 2 and histograms in Figure 5). We are puzzled by the persistence of O_2^+ relative to N_2^+ and NO^+, species which have bond energies stronger than O_2, both as ions and neutral molecules (see Table S12 in the SI).

Figure 9c includes the data measured across regimes on the 37 orbits of low to moderate solar/geomagnetic conditions that were selected for their low Mass-30 ion conditions (Christon et al., 2017; see also Figure S5) and used to construct the traces in Figure 7a. Comparison of this study's farthest upstream data (black histogram) to that from the cross-regime 37-orbit collection (blue histogram) and the long-term SPHERE distribution (red histogram) demonstrates that both lunar-origin Si^+ and ionospheric-origin O_2^+ are likely present in the upstream data. Si^+ is both an ionospheric origin metal ion derived from IDPs (Plane et al., 2016; Zbinden et al., 1975) and a prominent lunar pickup ion (e.g., Halekas et al., 2015; Mall et al., 1998; Poppe et al., 2016). Although the quiet interval data show overall similarity to the farthest upstream data, evidence of a peak at Mg^+ and at Na^+ (both possibly from the ionosphere's meteoric metal ion layers), but not necessarily at Al^+ or P^+ (likely lunar pickup ions), argues more strongly for an ionospheric ion dominance and somewhat against a lunar pickup ion dominance in these multiregime data obtained during low-to-moderate geomagnetic activity. Mg^+, a well-known ionospheric IDP origin ion, has not been clearly identified in lunar PUI (Halekas et al., 2015; Poppe et al., 2016).

5. Discussion and Summary

Important new information on suprathermal atomic and molecular ions in and near the magnetospheres of Earth, Jupiter, and Saturn is presented in this paper. Although the principal intended subject of the paper did not initially include atomic ions, establishing characteristics of some atomic ions in and near the three magnetospheres, for example, a focus on S^+ at Jupiter and the characterization of some aspects of lunar pickup ions near Earth, was essential in more fully, and we hope more accurately, describing magnetospheric molecular ions at Earth and Saturn. We discuss our results in that context, with our primary focus on the molecules and only supplementary reportage on atomic ions as is relevant to this survey at this juncture.

5.1. Jupiter

Cassini was in the Jovian magnetosphere for far too short an interval for CHEMS to obtain detailed composition measurements. Nevertheless, review of the Cassini/CHEMS cruise data within ~2 AU of Jupiter shows the wide extent of Jovian-origin S^+ in the solar system. The suprathermal S^+ flux observed in interplanetary space no doubt contains some ions that were energized in and escaped from the Jovian magnetosphere. However, another strong source arises from energetic neutral S atoms escaping from Jupiter before being ionized and picked up by the solar wind, as modeled by Luhmann (2003). The pickup S^+ ion cutoff energy for 400 km/s solar wind is nearly 100 keV, easily observed by the CHEMS instrument. Inside this possible Jovian S^+ PUI cloud, CHEMS observed S^+ sporadically in interplanetary space from ~4.3 to ~6.6 AU heliocentric (see Figures S12 and S1b in the SI), but not outside of that heliocentric distance range (that is, before ~2000-246 or after ~2002-001). We therefore feel that at the level so far investigated, our S^+ observations are generally consistent with Luhmann's S^+ PUI model. Even though the data are sparse, the basic unnormalized S^+ interplanetary observations herein may help interested researchers refine their interplanetary transport models. We noted above that a small amount of Ca^+ and a possible trace of CO_2^+ may be present in and near Jupiter's magnetosphere. This Ca^+ and CO_2^+, and likely O^+, may escape from Jupiter's magnetosphere as S^+ clearly does, and some interplanetary/interstellar PUI O^+ likely enters Jupiter's magnetosphere, further complicating relative abundance comparisons used in evaluating magnetospheric sources and escape scenarios. Other Jupiter-related MI, such as SO^+ from Io and/or O_2^+ from the Galilean satellites, for example, may be ejected into the magnetosphere but are more weakly bound than CO_2^+ (see Table S6 in the SI) and do not appear to survive in the harsh Jovian environment. Magnetospheric Jovian SO^+ and O_2^+ are not evident in our observations at suprathermal energies. The approximately equal amounts of O^+ and S^+ shown in Figure 3a argue for radiolysis of sulfur-based molecules as a source, with little contribution from the other possible O^+ sources, the water-ice Galilean satellites. However, full accounting of higher O and S charge states consistent with satellite source modeling may decide the true proportion of O^+ and S^+ derived from SO^+.

5.2. Saturn

Of the ion species identified at up to ~35–40 amu/e inside Saturn's magnetosphere, all but Fe^+ appear to escape, but at or with different rates, paths, or modes. Of note, Fe^+ is not observed in the Solar Wind samples collected for this study. Further review of the complete Sheath and Solar Wind data near Saturn will be needed to expand discussion of this topic. Figures 4 and 5 summarize the new information about MI at Saturn. Although we do not explore details of MI dissociation herein, we suggest that the robust decrease of H_2O^+ relative to O^+ may result from either strong H_2O^+ impact dissociation in the solar wind or from differences in escape or transport processes. Both $^{28}M^+$ and O_2^+ appear to have fewer losses escaping Saturn's magnetosphere than C^+, N^+, and O^+, in that the overall MI levels relative to O^+ are higher in the Solar Wind than in the Sphere unlike the atomic ions whose levels relative to O^+ are the same in both plasma regimes. This will all need to be sorted out when accurate instrumental efficiencies for these MI are applied and differential intensities are evaluated.

5.3. Earth

An important portion of this paper has been devoted to first establishing and characterizing the importance of the Mass-30 lunar PUI Al^+, Si^+, and P^+ that are present in the near-Earth environs outside the magnetosphere and subsequently treating the lunar PUI as the background they are in this study of Earth's MI. We roughly quantified the ratios of N_2^+, NO^+, and O_2^+ that flow out of the ionosphere into Earth's magnetosphere, showing that, relatively, the components of the magnetospheric MI population are roughly ~43% N_2^+, ~47% NO^+, and ~10% O_2^+. While demonstrating the separation of several lunar PUI from escaped ionospheric N_2^+ in our solar wind data, we found possible evidence of a lunar Fe^{+2} PUI component. During low geomagnetic activity levels when lower levels of MI are present, Si^+, very difficult to differentiate from the MI signal, is likely present at levels comparable to Fe^+ in these select intervals, consistent with an ionospheric source for both. Si^+ would be far more evident than Fe^+ if their source was the Moon, because repeated in situ efforts to measure Fe^+ near the Moon have produced null results, whereas, Si^+ is readily observed as a principal lunar PUI. This study was our first opportunity to characterize and investigate these mixed distributions, given the rarity and low count levels of some of these ions and the need for sufficient data to make statistically sound relative species proportion estimates. It is clear that ionospheric origin molecular ions escape into the SHEATH and then into the SW/IM sunward of the bow shock, and it is likely that they also travel at least ~10–15 Re sunward of the nose of the bow shock into the upstream solar wind at 1 AU.

6. Concluding Remarks

This paper provides new details regarding the molecular and atomic suprathermal heavy ion composition in and near three important magnetospheres in the solar system, those of Earth, Saturn, and Jupiter. In the largest magnetosphere, that of Jupiter, S^+ and O^+ from dissociated Iogenic molecular S and O compounds and, possibly O^+ from its icy moons are dominant. Jovian S^+ escapes into the interplanetary medium. Tentatively identified CO_2^+ may originate in, survive in, and escape from Jupiter's magnetosphere. At Saturn, the icy moons and rings are the likely sources of its most prominent ions, O^+, H_2O^+, O_2^+, and $^{28}M^+$. While C^+, N^+, O^+, OH^+, H_2O^+, $^{28}M^+$, and O_2^+ all escape from Saturn's magnetosphere, Fe^+ is not detected in the Solar Wind near Saturn, and we do not attempt to estimate the relative OH^+ abundance herein. The overall ratio of H_2O^+ relative to O^+ decreases in interplanetary space; all other ion's overall ratios to O^+ are ≥1. H_2O^+

must either dissociate more quickly than the $^{28}M^+$ and O_2^+, or its transport characteristics might constrain its escape more than for these two heavier molecules. At Earth, heavy ions observed inside the magnetosphere are dominated by those of ionospheric origin. Lunar origin ions are not detected at significant levels in the magnetosphere, except in the magnetospheric lobes where Mass-40 lunar Ca^+ and CO_2^+ PUI are detected. We demonstrate that the dominant heavy lunar PUI, Si^+, constitutes, at best, a negligible contribution to the long-term averaged suprathermal magnetospheric Mass-30 ion population. Our measurements of magnetospheric molecular ions, N_2^+ and NO^+ each ~43–46%, and O_2^+ ~10%, all originating in Earth's ionosphere, suggest that geomagnetic storms at Earth typically do not extract ions from ionospheric altitudes much lower or higher than ~300–500 km over the long term, that is, altitudes low enough to allow sufficient amounts of O_2^+ to escape, balanced with dominant, approximately equal, N_2^+ and NO^+ contributions.

Glossary of Acronyms and Terms

BR*	: Basic Rate M-vs-M/Q collection region (where * is 0–2 for STICS and 0–6 for CHEMS)
CHEMS	: the Charge-Energy-Mass ion composition Spectrometer on the Cassini spacecraft
CIR	: large-scale, fast/slow solar wind stream interaction regions that corotate with the Sun
CME	: Coronal Mass Ejection—large-scale solar plasma flux that propagates in the solar wind
E	: total ion kinetic energy
E/Q	: total ion energy per charge
Em	: energy deposited in the solid-state detector by an incident ion
EPIC	: the energetic particle experiment on the Geotail spacecraft in Earth orbit
escape	: the process of magnetospheric ions exiting the magnetospheres of their origination
EUV	: Extreme Ultraviolet high-energy electromagnetic radiation naturally generated by the Sun, which affects planetary atmospheres and ionospheres
F10.7	: a measurement of the 10.7 cm radio flux RF emissions from the Sun, approximately correlated with solar EUV flux
IDP	: Interplanetary Dust Particle (dust, small asteroids, meteoroids, and comet particulates)
io … , pu … , sw …	: prefixes distinguishing ionosphere, pickup, and solar wind source ions
Kp	: geomagnetic activity index
livetime correction	: procedure used in calculating ion fluxes using PHAs and Basic Rates
LOBE	: part of magnetosphere where magnetic field pressure dominates over plasma pressure
LPUI	: a lunar origin PUI
M	: ion mass determined instrumentally from energy deposit, TOF, and E/Q
M/Q	: mass per charge determined instrumentally from TOF and E/Q
magnetosheath	: solar wind region between magnetosphere and bow shock in solar wind
magnetosphere	: region where planetary magnetic fields dominate
Mass-16 ions ($^{16}M^+$)	: Earth: N^+, O^+; Jupiter: O^+; Saturn: C^+, N^+, O^+, OH^+, H_2O^+, H_3O^+
Mass-20 ions ($^{20}M^+$)	: Earth, Moon, Jupiter, Saturn, Interplanetary: Ne^+, Na^+, Mg^+
Mass-30 ions ($^{30}M^+$)	: Earth (Moon): N_2^+, NO^+, Al^+, Si^+, P^+; Jupiter: S^+; Saturn: $^{28}M^+$, O_2^+
Mass-40 ions ($^{40}M^+$)	: Earth (Moon): K^+, Ar^+, Ca^+, CO_2^+, SiO^+, Ti^+; Jupiter: CO_2^+, SO^+; Saturn: $Ar^+\Vert Ca^+$, CO_2^+
MIMI	: the energetic particle experiment on the Cassini spacecraft
$^{28}MQ^+$	: Saturn's ~28–30 amu/e molecular ions, which could be one or more of the $^{28}M^+$ ions
$^{28}M^+$	: one, or a combination, of CO^+, N_2^+, $HCNH^+$, and $C_2H_4^+$
outflow	: the process in which ions exit (flow out of) the ionosphere of their origination
PHA	: a Pulse Height Analyzed ion event sample of all ions measured by STICS or CHEMS

prime Fe PHA	: a Fe PHA event in a restricted M and MPQ analysis range
PUI	: a PickUp Ion, an initially neutral particle ionized and picked up by the solar wind
Q	: charge (charge state) of an ion
RID	: an acronym for plasma Regime IDentification, only used in the Supporting Information
SHEATH	: turbulent, shocked solar wind plasma region between magnetopause and bow shock
Solar Cycle	: the ~11-year disturbance activity cycle of the Sun
SPHERE	: parts of magnetosphere where particle pressure dominates over magnetic pressure
STICS	: SupraThermal Ion Composition Spectrometer charge-energy-mass ion composition spectrometers on the Geotail and WIND spacecraft
SW, SH, SP, LB	: two-letter acronyms for the SW/IM, SHEATH, SPHERE, and LOBE names
SW/IM	: unshocked solar wind, interplanetary medium outside the bow shock
TOF	: time of flight measured instrumentally
Vsw	: solar wind speed
W^+	: ion group containing O^+, OH^+, H_2O^+, and H_3O^+

Acknowledgments

We thank George Gloeckler who conceived the STICS and CHEMS spectrometers and directed their development at the University of Maryland Space Physics Group. Their excellent performance and long lifetimes made this study possible. This work would not exist without the encouragement of R. W. McEntire and D. J. Williams and help of S. Lasley, R. DiFabio, J. Gunther, J. Cain, E. Tums, P. Wilson, O. Lamm, and many others. We thank NASA for support through Grants NNX13AE61G and NNN06AA01C(NA07). J. M. C. P.'s work was supported by the European Research Council (project 291332-CODITA). We thank C. W. Kelly (University of Leeds) for providing WACCM-X data. We acknowledge the use of the list of Cassini magnetopause and bow shock crossings compiled by H. J. McAndrews, S. J. Kanani, A. Masters, and J. C. Cutler. The NASA Plasma Region identifications for Geotail's orbital locations in and near Earth's magnetosphere were invaluable in this research. The Geotail/EPIC/STICS data set for 1992 through 2010 can be found at http://spdf.gsfc.nasa.gov/pub/data/geotail/epic/stics_pha_ascii_gzip/and for later times at http://sd-www.jhuapl.edu/Geotail/. Geotail ephemeris data are at http://sscweb.gsfc.nasa.gov/. Solar and geomagnetic indices were obtained from both http://omniweb.gsfc.nasa.gov/form/dx1.html and http://wdc.kugi.kyoto-u.ac.jp/dstae/. The entire Cassini/MIMI/CHEMS data set and Cassini ephemeris data can be found at http://pds.nasa.gov. S.P.C. thanks H.T. Smith for useful discussions about the continuing investigation into the Titan Torus. S. P. C. thanks J. M. Huba for a helpful discussion about the SAMI3 Model, which was developed by J. Huba, G. Joyce, and M. Swisdak of the Plasma Physics Division, Naval Research Laboratory and Icarus Research, Inc. SAMI3 simulation results are provided by the Community Coordinated Modeling Center at Goddard Space Flight Center through their public Runs on Request system (http://ccmc.gsfc.nasa.gov).

References

Allen, R. C., Mitchell, D. G., Paranicas, C. P., Hamilton, D. C., Clark, G., Rymer, A. M., et al. (2018). Internal versus external sources of plasma at Saturn: Overview from Magnetospheric Imaging Investigation/Charge-Energy-Mass Spectrometer data. *Journal of Geophysical Research: Space Physics*, *123*, 4712–4727. https://doi.org/10.1029/2018JA025262

Andersson, L., Peterson, W. K., & McBryde, K. M. (2004). Dynamic coordinates for auroral ion outflow. *Journal of Geophysical Research*, *109*, A08201. https://doi.org/10.1029/2004JA010424

André, M., & Cully, C. M. (2012). Low-energy ions: A previously hidden solar system particle population. *Geophysical Research Letters*, *39*, L03101. https://doi.org/10.1029/2011GL050242

Arista, N. R. (2000). Stopping of molecules and clusters. *Nuclear Instruments and Methods in Physics Research, B*, *164*, 108–138. https://doi.org/10.1016/S0168-583X(99)01069-1

Baluikin, I. I., Bertaux, J.-L., Quémerais, E., Izmodenov, V. V., & Schmidt, W. (2019). SWAN/SOHO Lyman-a-mapping: Hydrogen Geocorona extends far beyond the moon. *Journal of Geophysical Research: Space Physics*, *124* (accepted, 861–885. https://doi.org/10.1029/2018JA026136

Blagoveshchenskii, D. V. (2013). Effect of geomagnetic storms (substorms) on the ionosphere: 1. A review. *Geomagnetism and Aeronomy*, *53*(3), 275–290. https://doi.org/10.1134/S0016793213030031

Bockelée-Morvan, D. (2011). An overview of comet composition. In J. Cernicharo, & R. Bachiller (Eds.), *IAU Symposium 280, The Molecular Universe*, (pp. 261–274). Cambridge: Cambridge Univ. Press. https://doi.org/10.1017/S1743921311025038

Bodisch, K. M., Dougherty, L. P., & Bagenal, F. (2017). Survey of Voyager plasma science ions at Jupiter: 3. Protons and minor ions. *Journal of Geophysical Research: Space Physics*, *122*, 8277–8294. https://doi.org/10.1002/2017JA024148

Borovsky, J. E., & Denton, M. H. (2006). Effect of plasmaspheric drainage plumes on solar-wind/magnetosphere coupling. *Geophysical Research Letters*, *33*, L20101. https://doi.org/10.1029/2006GL026519

Bridges, J. C., Burchell, M. J., Changela, H. C., Foster, N. J., Cre, J. A., Carpenter, J. D., et al. (2010). Iron oxides in comet 81P/Wild 2. *Meteoritics and Planetary Science*, *45*(1), 55–72. https://doi.org/10.1111/j.1945-5100.2009.01

Campbell, R. D., & Lin, R. P. (1973). Energy loss of low energy nuclei in silicon surface barrier detectors. *The Review of Scientific Instruments*, *44*(10), 1510–1512. https://doi.org/10.1063/1.1685986

Cannata, R. W. (1990). Thermal ion upwelling in the High-Latitude Ionosphere (Doctoral dissertation). Retrieved from Deep Blue. (https://deepblue.lib.umich.edu/handle/2027.42/104904). Ann Arbor, MI: University of Michigan.

Carlson, R. W. (1999). A tenuous carbon dioxide atmosphere on Jupiter's moon Callisto. *Science*, *283*(5403), 820–821. https://doi.org/10.1126/science.283.5403.820

Carrillo-Sánchez, J. D., Nesvorný, D., Pokorný, P., Janches, D., & Plane, J. M. C. (2016). Sources of cosmic dust in the Earth's atmosphere. *Geophysical Research Letters*, *43*, 11,979–11,986. https://doi.org/10.1002/2016GL071697

Christon, S. P., Desai, M. I., Eastman, T. E., Gloeckler, G., Kokubun, S., Lui, A. T. Y., et al. (2000). Low-charge-state heavy ions upstream of Earth's bow shock and sunward flux of ionospheric O^{+1}, N^{+1}, and O^{+2} ions: Geotail observations. *Geophysical Research Letters*, *27*, 2433–2436. https://doi.org/10.1029/2000GL000039

Christon, S. P., Gloeckler, G., Williams, D. J., Mukai, T., McEntire, R. W., Jacquey, C., et al. (1994). Energetic atomic and molecular ions of ionospheric origin observed in distant magnetotail flow-reversal events. *Geophysical Research Letters*, *21*(25), 3023–3026. https://doi.org/10.1029/94GL02095

Christon, S. P., Hamilton, D. C., DiFabio, R. D., Mitchell, D. G., Krimigis, S. M., & Jontof-Hutter, D. S. (2013). Saturn suprathermal O_2^+ and mass-28^+ molecular ions: Long-term seasonal and solar variation. *Journal of Geophysical Research: Space Physics*, *118*, 3446–3463. https://doi.org/10.1002/jgra.50383

Christon, S. P., Hamilton, D. C., Gloeckler, G., Eastman, T. E., & Ipavich, F. M. (1994). High charge state carbon and oxygen ions in Earth's equatorial quasi-trapping region. *Journal of Geophysical Research*, *99*(A7), 13,465–13,488. https://doi.org/10.1029/93JA0332

Christon, S. P., Hamilton, D. C., Mitchell, D. G., DiFabio, R. D., & Krimigis, S. M. (2014). Suprathermal magnetospheric minor ions heavier than water at Saturn: Discovery of $^{28}M^+$ seasonal variations. *Journal of Geophysical Research: Space Physics*, *119*, 5662–5673. https://doi.org/10.1002/2014JA020010

Christon, S. P., Hamilton, D. C., Mitchell, D. G., Krimigis, S. M., & DiFabio, R. D. (2013). Minor and rare suprathermal heavy ions in Saturn's magnetosphere. See original copy in supporting information. Paper presented at American Geophysical Union 2013 Fall Meeting, Abstract: SM21A-2162. http://adsabs.harvard.edu/abs/2013AGUFMSM21A2162

Christon, S. P., Hamilton, D. C., Plane, J. M. C., Mitchell, D. G., DiFabio, R. D., & Krimigis, S. M. (2015). Discovery of suprathermal Fe^+ in Saturn's magnetosphere. *Journal of Geophysical Research: Space Physics*, *120*, 2720–2738. https://doi.org/10.1002/2014JA020906

Christon, S. P., Hamilton, D. C., Plane, J. M. C., Mitchell, D. G., Grebowsky, J. M., Spjeldvik, W. N., & Nylund, S. R. (2017). Discovery of suprathermal ionospheric origin Fe^+ in and near Earth's magnetosphere. *Journal of Geophysical Research: Space Physics*, *122*, 11,175–11,200. https://doi.org/10.1002/2017JA024414

Christon, S. P., Mall, U., Eastman, T. E., Gloeckler, G., Lui, A. T. Y., McEntire, R. W., & Roelof, E. C. (2002). Solar cycle and geomagnetic N^{+1}/O^{+1} variation in outer dayside magnetosphere: Possible relation to topside ionosphere. *Geophysical Research Letters*, *29*(5), 1058. https://doi.org/10.1029/2001GL013988

Cohen, I. J., Mauk, B. H., Anderson, B. J., Westlake, J. H., Sibeck, D. G., Giles, B. L., et al. (2016). Observations of energetic particle escape at the magnetopause: Early results from the MMS Energetic Ion Spectrometer (EIS). *Geophysical Research Letters*, *43*, 5960–5968. https://doi.org/doi:10.1002/2016GL068689

Cooper, J. F., Johnson, R. E., Mauk, B. H., Garrett, H. B., & Gehrels, N. (2001). Energetic ion and electron irradiation of the icy Galilean satellites. *Icarus*, *149*(1), 133–159. https://doi.org/10.1006/icar.2000.6498

Craven, P. D., Olsen, R. C., Chappell, C. R., & Kakani, L. (1985). Observations of molecular ions in the Earth's magnetosphere. *Journal of Geophysical Research*, *90*(A8), 7599–7605. https://doi.org/10.1029/JA090iA08p07599

Danilov, A. D., & Lastovica, J. (2001). Effects of geomagnetic storms on the ionosphere and atmosphere. *International Journal of Geomagnetism and Aeronomy*, *2*(3), 209–224. http://elpub.wdcb.ru/journals/ijga/v02/gai99312/gai99312.htm

DiFabio, R. D. (2012). *Spatial and temporal variations of the suprathermal (3-220 keV/e) ion composition in Saturn's equatorial magnetosphere (Doctoral dissertation)*. Retrieved from Digital Repository at the University of Maryland. College Park, Maryland, USA: University of Maryland. https://drum.lib.umd.edu/handle/1903/12700

DiFabio, R. D., Hamilton, D. C., Krimigis, S. M., & Mitchell, D. G. (2011). Long term time variations of the suprathermal ions in Saturn's magnetosphere. *Geophysical Research Letters*, *38*, L18103. https://doi.org/:10.1029/2011GL048841

Dukes, C. A., & Baragiola, R. A. (2015). The lunar surface-exosphere connection: Measurement of secondary-ions from Apollo soils. *Icarus*, *255*, 51–57. https://doi.org/10.1016/j.icarus.2014.11.032

Eckardt, J. C., Lantschner, G., Arista, N. R., Baragiola, R., & Baragiola, A. (1978). Electronic stopping of slow molecular ions in solids. *Journal of Physics C: Solid State Physics*, *11*(21), L851–L855. https://doi.org/doi:10.1088/0022-3719/11/21/001

Elphic, R. C., Funsten, H. O. III, Barraclough, B. L., McComas, D. J., Paffett, M. T., Vaniman, D. T., & Heiken, G. (1991). Lunar surface composition and solar wind-induced secondary ion mass spectrometry. *Geophysical Research Letters*, *18*, 2165–2168. https://doi.org/10.1029/91GL02669

Farrugia, C. J., Young, D. T., Geiss, J., & Balsiger, H. (1989). The composition, temperature, and density structure of cold ions in the quiet terrestrial plasmasphere: GEOS 1 results. *Journal of Geophysical Research*, *94*(A9), 11,865. https://doi.org/10.1029/JA094iA09p11865

Foss, V., Yau, A. W., & Shizgal, B. (2017). Molecular ions in ion upflows and their effects on hot atomic oxygen production. Paper presented at American Geophysical Union Fall Meeting 2017, abstract #SA43B-2654. http://adsabs.harvard.edu/abs/2017AGUFMSA43B2654F

Fujimoto, M., Nishida, A., Mukai, T., Saito, Y., Yamamoto, T., & Kokubun, S. (1996). Plasma entry from the flanks of the near-Earth magnetotail: GEOTAIL observations in the dawnside LLBL and the plasma sheet. *Journal of Geomagnetism and Geoelectricity*, *48*(5), 711–727. https://doi.org/10.5636/jgg.48.711

Fujimoto, M., Terasawa, T., Mukai, T., Saito, Y., Yamamoto, T., & Kokubun, S. (1998). Plasma entry from the flanks of the near-Earth magnetotail: Geotail observations. *Journal of Geophysical Research*, *103*, 4391–4408. https://doi.org/10.1029/97JA03340

Geiss, J., Gloeckler, G., Balsiger, H., Fisk, L. A., Galvin, A. B., Gliem, F., et al. (1992). Plasma composition in Jupiter's magnetosphere—Initial results from the Solar Wind Ion Composition Spectrometer. *Science*, *257*(5076), 1535–1539. https://doi.org/10.1126/science.257.5076.1535

Gilbert, J. A., Lepri, S. T., Landi, E., & Zurbuchen, T. H. (2012). First measurements of the complete heavy-ion charge state distributions of C, O, and Fe associated with interplanetary coronal mass ejections. *Astrophysical Journal*, *751*(20), 1–8. https://doi.org/10.1088/0004-637X/751/1/20

Gloeckler, G., Balsiger, H., Bürgi, A., Bochsler, P., Fisk, L. A., Galvin, A. B., et al. (1995). The solar wind and suprathermal ion composition investigation on the WIND spacecraft. *Space Science Reviews*, *71*(1–4), 79–124. https://doi.org/10.1007/BF00751327

Gloeckler, G., Fisk, L. A., Geiss, J., Schwadron, N. A., & Zurbuchen, T. H. (2000). Elemental composition of the inner source pickup ions. *Journal of Geophysical Research*, *105*, 7459–7463. https://doi.org/10.1029/1999JA000224

Gloeckler, G., Fisk, L. A., Zurbuchen, T. H., & Schwadron, N. A. (2000). Sources, injection and acceleration of heliospheric ion populations. In R. Mewaldt, et al. (Eds.), *AIP Conference Proceedings, CP528: Acceleration and Transport of Energetic Particles Observed in the Heliosphere: ACE 2000 Symposium* (pp. 221–228). United States: American Institute of Physics. https://doi.org/10.1063/1.1324316

Gloeckler, G., & Hamilton, D. C. (1987). AMPTE ion composition results. *Physica Scripta*, *T18*, 73–84. https://doi.org/10.1088/0031-8949/1987/T18/009

Gomis, O., & Strazzulla, G. (2005). CO_2 production by ion irradiation of H_2O ice on top of carbonaceous materials and its relevance to the Galilean satellites. *Icarus*, *177*(2), 570–576. https://doi.org/10.1016/j.icarus.2005.04.003

Goncharenko, L. P., Salah, J. E., Foster, J. C., & Huang, C. (2004). Variations in lower thermosphere dynamics at midlatitudes during intense geomagnetic storms. *Journal of Geophysical Research*, *109*, A04304. https://doi.org/10.1029/2003JA010244

Grebowsky, J. M., & Aikin, A. C. (2002). In situ measurements of meteoric ions. In E. Murad, & I. P. Williams (Eds.), *Meteors in the Earth's Atmosphere*, (pp. 189–214). Cambridge: Cambridge Univ. Press.

Haaland, S., Eriksson, A., Engwall, E., Lybekk, B., Nilsson, H., Pedersen, A., et al. (2012). Estimating the capture and loss of cold plasma from ionospheric outflow. *Journal of Geophysical Research*, *117*, A07311. http://doi.org/10.1029/2012JA017679

Haggerty, D. K., Hill, M. E., McNutt, R. L. Jr., & Paranicas, C. (2009). Composition of energetic particles in the Jovian magnetotail. *Journal of Geophysical Research*, *114*, A02208. https://doi.org/10.1029/2008JA013659

Halekas, J. S., Benna, M., Mahaffy, P. R., Elphic, R. C., Poppe, A. R., & Delory, G. T. (2015). Detections of lunar exospheric ions by the LADEE neutral mass spectrometer. *Geophysical Research Letters*, *42*, 5162–5169. https://doi.org/10.1002/2015GL064746

Heredia-Avalos, S., & Garcia-Molina, R. (2007). Reduction of the energy loss of swift molecular ions in solids due to vicinage effects in the charge state. *Physical Review A*, *76*(3), 032902. https://doi.org/doi:10.1103/PhysRevA.76.032902

Hibbitts, C. A., McCord, T. B., & Hansen, G. B. (2000). Distributions of CO_2 and SO_2 on the surface of Callisto. *Journal of Geophysical Research*, *105*, 22,541–22,558. https://doi.org/10.1029/1999JE001101

Hilchenbach, M., Hovestadt, D., Klecker, B., & Moebius, E. (1992). Detection of singly ionized lunar pick-up ions upstream of the Earth's bow shock. in Solar Wind Seven; Proceedings of the 3rd COSPAR Colloquium, Goslar, Germany, Sept. 16-20, 1991 (A93-33554 13-92), p. 349-355.

Hoegy, W. R., Grebowsky, J. M., & Brace, L. H. (1991). Ionospheric ion composition from satellite measurements made during 1970–1980: Altitude profiles. *Advances in Space Research*, *11*, 173–182. https://doi.org/10.1016/0273-1177(91)90340-P

Huba, J. D., Joyce, G., & Fedder, J. A. (2000). Sami2 is another model of the ionosphere (SAMI2): A new low-latitude ionosphere model. *Journal of Geophysical Research*, *105*(A10), 23,035–23,053. https://doi.org/10.1029/2000JA000035

Huba, J. D., Joyce, G., & Krall, J. (2008). Three-dimensional equatorial spread F modeling. *Geophysical Research Letters*, *35*, L10102. https://doi.org/10.1029/2008GL033509

Ilie, R., & Liemohn, M. W. (2016). The outflow of ionospheric nitrogen ions: A possible tracer for the altitude-dependent transport and energization processes of ionospheric plasma. *Journal of Geophysical Research: Space Physics*, *121*, 9250–9255. https://doi.org/10.1002/2015JA022162

Ipavich, F. M., Lundgren, R. A., Lambird, B. A., & Gloeckler, G. (1978). Measurements of pulse-height defect in Au-Si detectors for H, He, C, N, O, Ne, Ar, Kr from ~2 to ~400 keV/nucleon. *Nuclear Instruments and Methods*, *154*, 291–294. https://doi.org/10.1016/0029-554X(78)90412-3

Johnson, R. E., Carlson, R. W., Cooper, J. F., Paranicas, C., Moore, M. H., & Wong, M. C. (2004). Radiation effects on the surfaces of the Galilean satellites. In F. Bagenal, T. E. Dowling, & W. B. McKinnon (Eds.), *Jupiter. The planet, satellites and magnetosphere*, *Cambridge Planetary Science* (Vol. 1, pp. 485–512). Cambridge, UK: Cambridge University Press. isbn: 0-521-81808-7

Kalescky, R., Kraka, E., & Cremer, D. (2013). Identification of the strongest bonds in chemistry. *Journal of Physical Chemistry A*, *117*(36), 8981–8995. https://doi.org/10.1021/jp406200w

Kallenbach, R., Geiss, J., Gloeckler, G., & von Steiger, R. (2000). Pick-up ion measurements in the heliosphere—A review. *Astrophysics and Space Science*, *274*, 97. https://doi.org/10.1023/A:1026587620772

Kim, Y. H., Pesnell, W. D., Grebowsky, J. M., & Fox, J. L. (2001). Meteoric ions in the ionosphere of Jupiter. *Icarus*, *150*(2), 261–278. https://doi.org/10.1006/icar.2001.6590

Kirsch, E., Wilken, B., Gloeckler, G., Galvin, A. B., Geiss, J., & Hovestadt, D. (1998). *Search for lunar pickup ions*, *COSPAR Colloquia Series* (Vol. 9, pp. 65–69). Beijing: Pergamon. https://doi.org/10.1016/S0964-2749(98)80011-5

Kis, A., Scholer, M., Klecker, B., Möbius, E., Lucek, E., Reme, A., et al. (2004). Multi-spacecraft observations of diffuse ions upstream of Earth's bow shock. *Geophysical Research Letters*, *31*, L20801. https://doi.org/10.1029/2004GL020759

Klecker, B., Möbius, E., Hovestadt, D., Scholer, M., Gloeckler, G., & Ipavich, F. M. (1986). Discovery of energetic molecular ions (NO^+ and $O_2{}^+$) in the storm ring current. *Geophysical Research Letters*, *13*, 632–635. https://doi.org/10.1029/GL013i007p00632

Köhnlein, W. (1989). A model of the terrestrial ionosphere in the altitude interval 50–4000 km: II. Molecular ions ($N_2{}^+$, NO^+, $O_2{}^+$) and electron density. *Earth, Moon, and Planets*, *47*(2), 109–163. https://doi.org/10.1007/BF00058139

Krimigis, S. M., Mitchell, D. G., Hamilton, D. C., Dandouras, J., Armstrong, T. P., Bolton, S. J., et al. (2002). A nebula of gases from Io surrounding Jupiter. *Nature*, *415*(6875), 994–996. https://doi.org/10.1038/415994a

Krimigis, S. M., Mitchell, D. G., Hamilton, D. C., Livi, S., Dandouras, J., & Jaskulek, et al. (2004). Magnetosphere Imaging Instrument (MIMI) on the Cassini mission to Saturn/Titan. *Space Science Reviews*, *114*, 233–329. https://doi.org/10.1007/s11214-004-1410-8

Kronberg, E. A., Bučík, R., Haaland, S., Klecker, B., Keika, K., Desai, M. I., et al. (2011). On the origin of the energetic ion events measured upstream of the Earth's bow shock by STEREO, Cluster, and Geotail. *Journal of Geophysical Research*, *116*, A02210. https://doi.org/10.1029/2010JA015561

Kunde, V. G., Flasar, F. M., Jennings, D. E., Bézard, B., Strobel, D. F., Conrath, B. J., et al. (2004). Jupiter's atmospheric composition from the Cassini Thermal Infrared Spectroscopy Experiment. *Science*, *305*(5690), 1582–1586. https://doi.org/10.1126/science.1100240

Kuppers, M., & Schneider, N. M. (2000). Discovery of chlorine in the Io torus. *Geophysical Research Letters*, *27*, 513–516. https://doi.org/10.1029/1999GL010718

Lennartsson, O. W., Collin, H. L., Ghielmetti, A. G., & Peterson, W. K. (2000). A statistical comparison of the outflow of NO^+, NO^+ and $O_2{}^+$ molecular ions with that of atomic O^+ ions using Polar/TIMAS observations. *Journal of Atmospheric and Solar-Terrestrial Physics*, *62*, 477–483. https://doi.org/10.1016/S1364-6826(00)00019-5

Liu, H.-L., Bardeen, C. G., Foster, B. T., Lauritzen, P., Liu, J., Lu, G., et al. (2018). Development and validation of the Whole Atmosphere Community Climate Model with thermosphere and ionosphere extension (WACCM-X 2.0). *Journal of Advances in Modeling Earth Systems*, *10*, 381–402. https://doi.org/10.1002/2017MS001232

Liu, H.-L., Foster, B. T., Hagan, M. E., McInerney, J. M., Maute, A., Qian, L., et al. (2010). Thermosphere extension of the Whole Atmosphere Community Climate Model. *Journal of Geophysical Research*, *115*, A12302. https://doi.org/10.1029/2010JA015586

Luhmann, J. G. (2003). Expected heliospheric attributes of Jovian pickup ions from the extended neutral gas disk. *Planetary and Space Science*, *51*, 387–392. https://doi.org/10.1016/S0032-0633(03)00034-5

Mahaffy, P. R., Niemann, H. B., Alpert, A., Atreya, S. K., Demick, J., Donahue, T. M., et al. (2000). Noble gas abundance and isotope ratios in the atmosphere of Jupiter from the Galileo Probe Mass Spectrometer. *Journal of Geophysical Research*, *105*(E6), 15,061–15,071. https://doi.org/10.1029/1999JE001224

Mall, U., Kirsch, E., Cierpka, K., Wilken, B., Soding, A., Neubauer, F., et al. (1998). Direct observation of lunar pick-up ions near the Moon. *Geophysical Research Letters*, *25*, 3799–3802. https://doi.org/10.1029/1998GL900003

Mall, U. A., Christon, S. P., Kirsch, E., & Gloeckler, G. (2002). On the solar cycle dependence of the N^+/O^+ content in the magnetosphere and its relation to atomic N and O in the Earth's exosphere. *Geophysical Research Letters*, *29*(12), 1593. https://doi.org/10.1029/2001GL013957

Mandt, K. E., Gell, D. A., Perry, M., Hunter Waite, J. Jr., Crary, F. A., Young, D., et al. (2012). Ion densities and composition of Titan's upper atmosphere derived from the Cassini Ion Neutral Mass Spectrometer: Analysis methods and comparison of measured ion densities to photochemical model simulations. *Journal of Geophysical Research*, *117*, E10006. https://doi.org/10.1029/2012JE004139

Martens, H. R., Reisenfeld, D. B., Williams, J. D., Johnson, R. E., & Smith, H. T. (2008). Observations of molecular oxygen ions in Saturn's inner magnetosphere. *Geophysical Research Letters*, *35*, L20103. https://doi.org/10.1029/2008GL035433

Mauk, B. H., Cohen, I. J., Haggerty, D. K., Hospodarsky, G. B., Connerney, J. E. P., Anderson, B. J., et al. (2019). Investigation of mass/charge-dependent escape of energetic ions across the magnetopauses of Earth and Jupiter. *Journal of Geophysical Research: Space Physics*, *124*, 5539–5567. https://doi.org/10.1029/2019JA026626

Mauk, B. H., Hamilton, D. C., Hill, T. W., Hospodarsky, G. B., Johnson, R. E., Paranicas, C., et al. (2009). Fundamental plasma processes in Saturn's magnetosphere, Chapter 11. In M. K. Dougherty, L. W. Esposito, & S. M. Krimigis, *Saturn from Cassini-Huygens* (1st ed., *11*, pp. 281–331). Heidelberg, Germany: Springer. https://doi.org/10.1007/978-1-4020-9217-6_11

McComas, D. J., Allegrini, F., Bochsler, P., Frisch, P., Funsten, H. O., Gruntman, M., et al. (2009). Lunar backscatter and neutralization of the solar wind: First observations of neutral atoms from the Moon. *Geophysical Research Letters*, *36*, L12104. https://doi.org/10.1029/2009GL038794

McEwen, A. S., Keszthelyi, L. P., Lopes, R., Schenk, P. M., & Spencer, J. R. (2007). The lithosphere and surface of Io. In F. Bagenal, T. E. Dowling, & W. B. McKinnon (Eds.), *Jupiter, The Planet, Satellites and Magnetosphere* (pp. 307–326). Cambridge, UK: Cambridge University Press. isbn: 9780521035453

McKenna-Lawlor, S., Li, L., Barabash, S., Kudela, K., Balaz, J., Strharsky, I., et al. (2005). The NUADU experiment on TC-2 and the first Energetic Neutral Atom (ENA) images recorded by this instrument. *Annales Geophysicae*, *23*, 2825–2849. https://doi.org/10.5194/angeo-23-2825-2005

Mitchell, D. G., Gkioulidou, M., & Ukhorskiy, A. Y. (2018). Energetic ion injections inside geosynchronous orbit: Convection- and drift-dominated, charge-dependent adiabatic energization (W = qEd). *Journal of Geophysical Research: Space Physics*, *123*, 6360–6382. https://doi.org/10.1029/2018JA025556

Mitchell, D. G., Roelof, E. C., Sanderson, T. R., Reinhard, R., & Wenzel, K.-P. (1983). ISEE/IMP observations of simultaneous upstream ion events. *Journal of Geophysical Research*, *88*, 5635–5644. https://doi.org/10.1029/JA088iA07p05635

Moore, T. E., Fok, M.-C., & Garcia-Sage, K. (2014). The ionospheric outflow feedback loop. *Journal of Atmospheric and Solar-Terrestrial Physics*, *115-116*, 59–66. https://doi.org/10.1016/j.jastp.2014.02.002

Nesvorný, D., Jenniskens, P., Levison, H. F., Bottke, W. F., Vokrouhlický, D., & Gounelle, M. (2010). Cometary origin of the zodiacal cloud and carbonaceous micrometeorites: Implications for hot debris disks. *Astrophysical Journal*, *713*(2), 816–836. https://doi.org/10.1088/0004-637X/713/2/816

Nishida, A. (1994). The GEOTAIL mission. *Geophysical Research Letters*, *21*(25), 2871–2873. https://doi.org/10.1029/94GL01223

Ogawa, Y., Buchert, S. C., Sakurai, A., Nozawa, S., & Fujii, R. (2010). Solar activity dependence of ion upflow in the polar ionosphere observed with the European Incoherent Scatter (EISCAT) Tromsø UHF radar. *Journal of Geophysical Research*, *115*, A07310. https://doi.org/10.1029/2009JA014766

Pan, Q. (2015). Charged particle energization and transport in the magnetotail during substorms. (Doctoral dissertation). Retrieved from eScholarship. (https://escholarship.org/uc/item/2056z0tq). Los Angeles, CA: University of California. Pub. Number: AAT 3719439; ISBN: 9781321997873

Peterson, W. K., Abe, T., Fukunishi, H., Greffen, M. J., Hayakawa, H., Kasahara, Y., et al. (1994). On the sources of energization of molecular ions at ionospheric altitudes. *Journal of Geophysical Research*, *99*(A12), 23,257–23,274. https://doi.org/10.1029/94JA01738

Peterson, W. K., Sharp, R. D., Shelley, E. G., Johnson, R. G., & Balsiger, H. (1981). Energetic ion composition of the plasma sheet. *Journal of Geophysical Research*, *86*, 761–767. https://doi.org/10.1029/JA086iA02p00761

Peterson, W. K., Tung, Y. K., Carlson, C. W., Clemmons, J. H., Collin, H. L., Ergun, R. E., et al. (1998). Simultaneous observations of solar wind plasma entry from FAST and POLAR. *Geophysical Research Letters*, *25*(12), 2081–2084. https://doi.org/10.1029/98GL00668

Plane, J. M. C. (2012). Cosmic dust in the Earth's atmosphere (Critical Review). *Chemical Society Reviews*, *41*, 6507–6518. https://doi.org/10.1039/C2CS35132C

Plane, J. M. C., Flynn, G. J., Määttänen, A., Moores, J. E., Poppe, A. R., Carrillo-Sanchez, J. D., & Listowski, C. (2018). Impacts of cosmic dust on planetary atmospheres and surfaces. *Space Science Reviews*, *214*(23), 1–42. https://doi.org/10.1007/s11214-017-0458-1

Plane, J. M. C., Gómez-Martín, J. C., Feng, W., & Janches, D. (2016). Silicon chemistry in the mesosphere and lower thermosphere. *Journal of Geophysical Research: Atmospheres*, *121*, 3718–3728. https://doi.org/10.1002/2015JD024691

Poppe, A. R. (2016). An improved model for interplanetary dust fluxes in the outer solar system. *Icarus*, *264*, 369–386. https://doi.org/10.1016/j.icarus.2015.10.001

Poppe, A. R., Halekas, J. S., Szalay, J. R., Horányi, M., Levin, Z., & Kempf, S. (2016). LADEE/LDEX observations of lunar pickup ion distribution and variability. *Geophysical Research Letters*, *43*, 3069–3077. https://doi.org/10.1002/2016GL068393

Posner, A., Schwadron, N. A., Zurbuchen, T. H., Kozyra, J. U., Liemohn, M. W., & Gloeckler, G. (2002). Association of low-charge-state heavy ions up to 200 Re upstream of the Earth's bow shock with geomagnetic disturbances. *Geophysical Research Letters*, *29*(7), 1099. https://doi.org/10.1029/2001GL013449

Postberg, F., Clark, R. N., Hansen, C., Coates, A., Daile Ore, C. M., Scipioni, F., et al. (2018). Plume and surface composition of Enceladus. In P. M. Schenk, et al. (Eds.), *Enceladus and the icy moons of Saturn* (pp. 129–162). Tucson, AZ: University of Arizona. https://doi.org/10.2458/azu_uapress_9780816537075-ch007

Price, G. D., & Jacka, F. (1991). The influence of geomagnetic activity on the upper mesosphere/lower thermosphere in the auroral zone: I. Vertical winds. *Journal of Atmospheric and Solar-Terrestrial Physics*, *53*(10), 909–922. https://doi.org/10.1016/0021-9169(91)90004-Q

Redmon, R. J., Peterson, W. K., Andersson, L., Richards, P. G., & Yau, A. W. (2014). An assessment of the role of soft electron precipitation in global ion upwelling. *Journal of Geophysical Research: Space Physics*, *119*, 7665–7678. https://doi.org/10.1002/2014JA020061

Richards, P. G. (2013). Solar cycle changes in the photochemistry of the ionosphere and thermosphere. In J. Huba, R. Schunk, & G. Khazanov (Eds.), *Modeling the ionosphere-thermosphere system* (Chap. 3, pp. 29–37). Chichester, UK: John Wiley, & Sons, Ltd. https://doi.org/10.1002/9781118704417.ch3

Sarantos, M., Hartle, R. E., Killen, R. M., Saito, Y., Slavin, J. A., & Glocer, A. (2012). Flux estimates of ions from the lunar exosphere. *Geophysical Research Letters*, *39*, L13101. https://doi.org/10.1029/2012GL052001

Scholer, M., Kucharek, H., & Giacalone, J. (2000). Cross-field diffusion of charged particles and the problem of ion injection and acceleration at quasi-perpendicular shocks. *Journal of Geophysical Research*, *105*, 18,285–18,293. https://doi.org/10.1029/1999JA000324

Seki, K., Keika, K., Kasahara, S., Yokota, S., Hori, T., Asamura, K., et al. (2019). Statistical properties of molecular ions in the ring current observed by the Arase (ERG) satellite. *Geophysical Research Letters*, *46*, 8643–8651. https://doi.org/doi:10.1029/2019GL084163

Shelley, E. G., Johnson, R. G., & Sharp, R. D. (1972). Satellite observations of energetic heavy ions during a geomagnetic storm. *Journal of Geophysical Research*, *77*(31), 6104–6110. https://doi.org/10.1029/JA077i031p06104

Shen, Y., Knudsen, D. J., Burchill, J. K., Howarth, A. D., Yau, A. W., Miles, D. M., et al. (2018). Low-altitude ion heating, downflowing ions, and BBELF waves in the return current region. *Journal of Geophysical Research: Space Physics*, *123*, 3087–3110. https://doi.org/10.1002/2017JA024955

Skjæveland, Å., Moen, J., & Carlson, H. C. (2014). Which cusp upflow events can possibly turn into outflows? *Journal of Geophysical Research: Space Physics*, *119*, 6876–6890. https://doi.org/10.1002/2013JA019495

Smith, H. T., & Rymer, A. M. (2014). An empirical model for the plasma environment along Titan's orbit based on Cassini plasma observations. *Journal of Geophysical Research: Space Physics*, *119*, 5674–5684. https://doi.org/10.1002/2014JA019872

Song, Y.-H., Wang, Y.-N., & Mišković, Z. L. (2005). Vicinage effects in energy loss and electron emission during grazing scattering of heavy molecular ions from a solid surface. *Physical Review A*, *72*(1), 012903. https://doi.org/10.1103/PhysRevA.72.012903

Sorathia, K. A., Merkin, V. G., Ukhorskiy, A. Y., Mauk, B. H., & Sibeck, D. G. (2017). Energetic particle loss through the magnetopause: A combined global MHD and test-particle study. *Journal of Geophysical Research: Space Physics*, *122*, 9329–9343. https://doi.org/10.1002/2017JA024268

Spjeldvik, W. N., & Rothwell, P. N. (1985). The radiation belts. In A. S. Jursa (Ed.), *Handbook of geophysics and the space environment*, edited by, (pp. 546–550). Hanscom AFB, MA, ADA 167 000, USA: Airforce Geophysics Laboratory. http://www.cnofs.org/Handbook_of_Geophysics_1985/Chptr05.pdf

Strangeway, R. J., Ergun, R. E., Su, Y.-J., Carlson, C. W., & Elphic, R. C. (2005). Factors controlling ionospheric outflows as observed at intermediate altitudes. *Journal of Geophysical Research*, *110*, A03221. https://doi.org/10.1029/2004JA010829

Strobel, D. F., & Yung, Y. L. (1979). The Galilean satellites as a source of CO in the Jovian upper atmosphere. *Icarus*, *37*(1), 256–263. https://doi.org/10.1016/0019-1035(79)90130-1

Tanaka, T., Saito, Y., Yokota, S., Asamura, K., Nishino, M. N., Tsunakawa, H., et al. (2009). First in situ observation of the Moon-originating ions in the Earth's magnetosphere by MAP-PACE on SELENE (KAGUYA). *Geophysical Research Letters*, *36*, L22106. https://doi.org/10.1029/2009GL040682

Tape, J. W., Gibson, W. M., Remillieu, J., Laubert, R., & Wegner, H. E. (1976). Energy loss of atomic and molecular ion beams in thin foils. *Nuclear Inststruments and Methods*, *132*, 75–77. https://doi.org/10.1016/0029-554X(76)90713-8

Taut, A., Berger, L., Drews, C., & Wimmer-Schweingruber, R. F. (2015). Composition of inner-source heavy pickup ions at 1 AU: SOHO/CELIAS/CTOF observations—Implications for the production mechanisms. *Astronomy and Astrophysics*, *576*(A55). https://doi.org/10.1051/0004-6361/201425139

Terasawa, T., Fujimoto, M., Mukai, T., Shinohara, I., Saito, Y., Yamamoto, T., et al. (1997). Solar wind control of density and temperature in the near-Earth plasma sheet: WIND/GEOTAIL collaboration. *Geophysical Research Letters*, *24*(8), 935–938. https://doi.org/10.1029/96GL04018

Thompson, M. S., Zega, T. J., Becerra, P., Keane, J. T., & Byrne, S. (2016). The oxidation state of nanophase Fe particles in lunar soil: Implications for space weathering. *Meteoritics, & Planetary Science*, *51*(6), 1082–1095. https://doi.org/10.1111/maps.12646

Verbischer, A. J., Skrutskie, M. F., & Hamilton, D. P. (2009). Saturn's largest ring. *Nature*, *461*, 1098–1100. https://doi.org/10.1038/nature08515

Vondrak, T., Plane, J. M. C., Broadley, S., & Janches, D. (2008). A chemical model of meteoric ablation. *Atmospheric Chemistry and Physics*, *8*(23), 7015–7031. https://doi.org/10.5194/acp-8-7015-2008

Waite, J. H. Jr., Combi, M. R., Ip, W.-H., Cravens, T. E., McNutt, R. L. Jr., Kasprzak, W., et al. (2006). Cassini ion and neutral mass spectrometer: Enceladus plume composition and structure. *Science*, *311*(5766), 1419–1422. https://doi.org/10.1126/science.1121290

Waite, J. H. Jr., Lewis, W. S., Magee, B. A., Lunine, J. I., McKinnon, W. B., Glein, C. R., et al. (2009). Liquid water on Enceladus from observations of ammonia and ^{40}Ar in the plume. *Nature*, *460*, 487–490. https://doi.org/10.1038/nature08153

Welling, D. T., & Liemohn, M. W. (2016). The ionospheric source of magnetospheric plasma is not a black box input for global models. *Journal of Geophysical Research: Space Physics*, *121*, 5559–5565. https://doi.org/10.1002/2016JA022646

Westlake, J. H., Paranicas, C. P., Cravens, T. E., Luhmann, J. G., Mandt, K. E., Smith, H. T., et al. (2012). The observed composition of ions outflowing from Titan. *Geophysical Research Letters*, *39*, L19104. https://doi.org/10.1029/2012GL05307

Westlake, J. H., Waite, J. H. Jr., Mandt, K. E., Carrasco, N., Bell, J. M., Magee, B. A., & Wahlund, J. -E. (2012). Titan's ionospheric composition and structure: Photochemical modeling of Cassini INMS data. *Journal of Geophysical Research*, *117*, E01003. https://doi.org/10.1029/2011JE003883

Williams, D. J., McEntire, R. W., Schlemm, C. II, Lui, A. T. Y., Gloeckler, G., Christon, S. P., & Gliem, F. (1994). Geotail energetic particles and ion composition instrument. *Journal of Geomagnetism and Geoelectricity*, *46*, 39–57. https://doi.org/10.5636/jgg.46.39

Wilson, G. R., Ober, D. M., Germany, G. A., & Lund, E. J. (2004). Nightside auroral zone and polar cap ion outflow as a function of substorm size and phase. *Journal of Geophysical Research*, *109*, A02206. https://doi.org/10.1029/2003JA009835

Wilson, J. K., Mendillo, M., & Baumgardner, J. (2002). The dual sources of Io's sodium clouds. *Icarus*, *157*, 476–489. https://doi.org/10.1006/icar.2002.6821

Woodson, A. K., Smith, H. T., Crary, F. J., & Johnson, R. E. (2015). Ion composition in Titan's exosphere via the Cassini Plasma Spectrometer I: T40 encounter. *Journal of Geophysical Research: Space Physics*, *120*, 212–234. https://doi.org/10.1002/2014JA020499

Yau, A. W., Howarth, A., Peterson, W. K., & Abe, T. (2012). Transport of thermal-energy ionospheric oxygen (O^+) ions between the ionosphere and the plasma sheet and ring current at quiet times preceding magnetic storms. *Journal of Geophysical Research*, *117*, A07215. https://doi.org/10.1029/2012JA017803

Yau, A. W., Peterson, W. K., & Abe, T. (2011). Influences of the ionosphere, thermosphere and magnetosphere on ion outflows. In W. Liu, & M. Fujimoto (Eds.), *The Dynamic Magnetosphere*, Edited by (pp. 283–314). Netherlands: Springer. https://doi.org/10.1007/978-94-007-0501-2_16

Yau, A. W., Whalen, B. A., Goodenough, C., Sagawa, E., & Mukai, T. (1993). EXOS D (Akebono) observations of molecular NO^+ and N_2^+ upflowing ions in the high-altitude auroral ionosphere. *Journal of Geophysical Research*, *98*(A7), 11,205–11,224. https://doi.org/10.1029/92JA02019

Yokota, S., & Saito, Y. (2005). Estimation of picked-up lunar ions for future compositional remote SIMS analyses of the lunar surface. *Earth, Planets and Space*, *57*(4), 281–289. https://doi.org/10.1186/BF03352564

Yu, Y., & Ridley, A. J. (2013). Exploring the influence of ionospheric O+ outflow on magnetospheric dynamics: Dependence on the source location. *Journal of Geophysical Research: Space Physics*, *118*, 1711–1722. https://doi.org/10.1029/2012JA018411

Zbinden, P. A., Hidalgo, M. A., Eberhahdt, P., & Geiss, J. (1975). Mass spectrometer measurements of the positive ion composition in the D- and E-regions of the ionosphere. *Planetary and Space Science*, *23*(12), 1621–1642. https://doi.org/10.1016/0032-0633(75)90090-2

References from the Supporting Information

Benna, M., Mahaffy, P. R, Halekas, J. S, Elphic, R. C, & Delory, G. T. (2015). Variability of helium, neon, and argon in the lunar exosphere as observed by the LADEE NMS instrument. *Geophysical Research Letters*, *42*, 3723–3729. https://doi.org/10.1002/2015GL064120

Bilitza, D., Altadil, D., Zhang, Y., Mertens, C., Truhlik, V., Richards, P., et al. (2014). The International Reference Ionosphere 2012—A model of international collaboration. *Journal of Space Weather and Space Climate*, *4*, A07. https://doi.org/10.1051/swsc/2014004

Bilitza, D., Rawer, K., Bossy, L., & Gulyaeva, T. (1993). International Reference Ionosphere—Past, present, and future: II. Plasma temperatures, ion composition and ion drift. *Advances in Space Research*, *13*(3), 15–23. https://doi.org/10.1016/0273-1177(93)90240-C

Burlaga, L. F., Lepping, R. P., Behannon, K. W., & Klein, L. W. (1984). Large-scale interplanetary magnetic fields: Voyager 1 and 2 observations between 1 AU and 9.5 AU. *Journal of Geophysical Research*, *89*, 10,659–10,668. https://doi.org/10.1029/JA089iA12p10659

Huba, J. D., Krall, J., & Joyce, G. (2009). Atomic and molecular ion dynamics during equatorial spread F. *Geophysical Research Letters*, *36*, L10106. https://doi.org/10.1029/2009GL037675

Kivelson, M. J., & Russell, C. T. (1995). *Introduction to Space Physics*, *Cambridge Atmospheric and Space Science Series* (p. 53). Cambridge, UK: Cambridge University Press.

Krupp, N., Woch, J., Lagg, A., Livi, S., Mitchell, D. G., Krimigis, S. M., et al. (2004). Energetic particle observations in the vicinity of Jupiter: Cassini MIMI/LEMMS results. *Journal of Geophysical Research*, *109*, A09S10. https://doi.org/10.1029/2003JA010111

Kurth, W. S, Gurnett, D. A, Hospodarsky, G. B., Farrell, W. M, Roux, A, Dougherty, M. K, Joy, S. P, et al. (2002). The dusk flank of Jupiter's magnetosphere. *Nature*, *415*(6875), 991–994.

Ruscic, B., Wagner, A. F., Harding, L. B., Asher, R. L., Feller, D., Dixon, D. A., Peterson, K. A., et al. (2002). On the enthalpy of formation of hydroxyl radical and gas-phase bond dissociation energies of water and hydroxyl. *Journal of Physical Chemistry A,*, *106*(11), 2727–2747. https://doi.org/10.1021/jp013909s

Smithtro, C. G., & Sojka, J. J. (2005). Behavior of the ionosphere and thermosphere subject to extreme solar cycle conditions. *Journal of Geophysical Research*, *110*, A08306. https://doi.org/10.1029/2004JA010782

Vandegrif, J., DiFabio, R., Hamilton, D., Kusterer, M., Manweiler, J., Mitchell, D., Paranicas, C., & Roussos, E. (2012). Cassini/MIMI Instrument Data User Guide. Washington, DC: NASA. Retrieved from http://pds.nasa.gov